Summer School "**Severe Convective Weather: Theory and Applications**"
Lecce, Italy, September 2012

IV. Atmospheric Boundary Layers in Pre-Storm Environments

Evgeni Fedorovich

University of Oklahoma, School of Meteorology

Outline

- **Convection initiation environments: interplay of mesoscale and boundary-layer scale forcings**

- **Convergence boundaries and horizontal convective rolls in pre-storm environments**

- **Characterization of sheared CBL: discrimination between cells and rolls**

- **Observed and simulated features of sheared CBL**

- **Boundary layer convection and formation of dust devils**

Necessary conditions for development of deep mesoscale convection
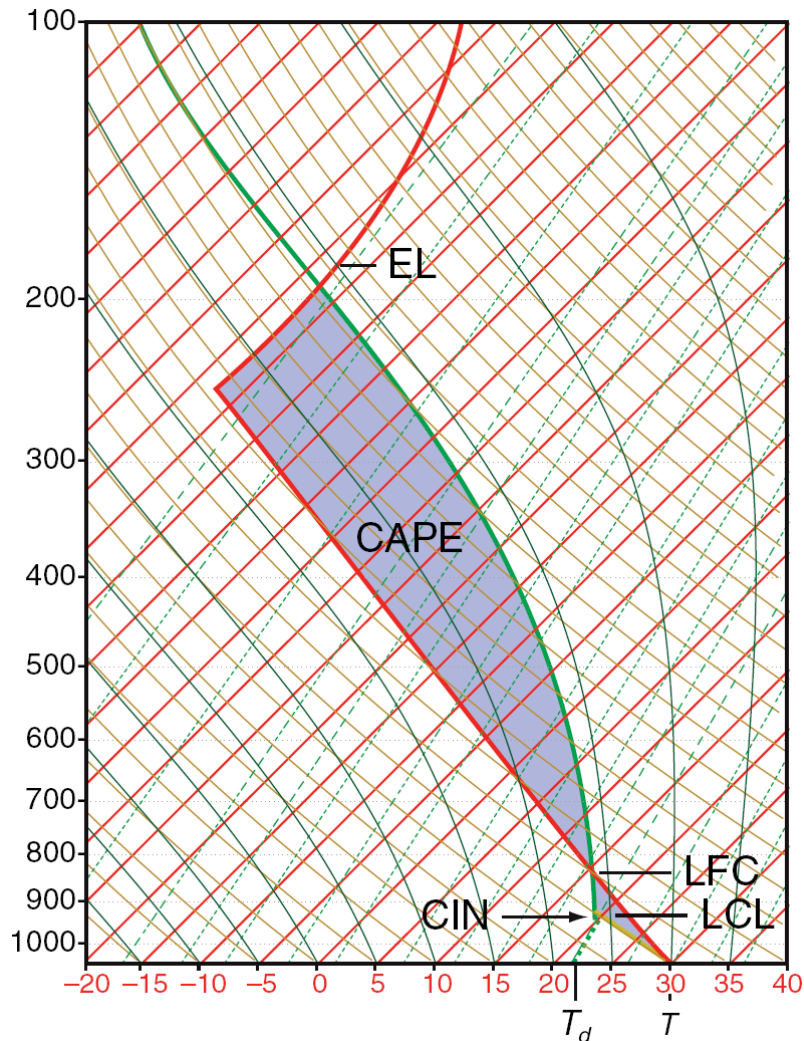
- **Existence of conditional unstable atmospheric layer with a significant vertical extension.**

  Temperature lapse rate must be larger than moist adiabatic lapse rate: $\Gamma_w < \Gamma = -dT/dz \le \Gamma_d$
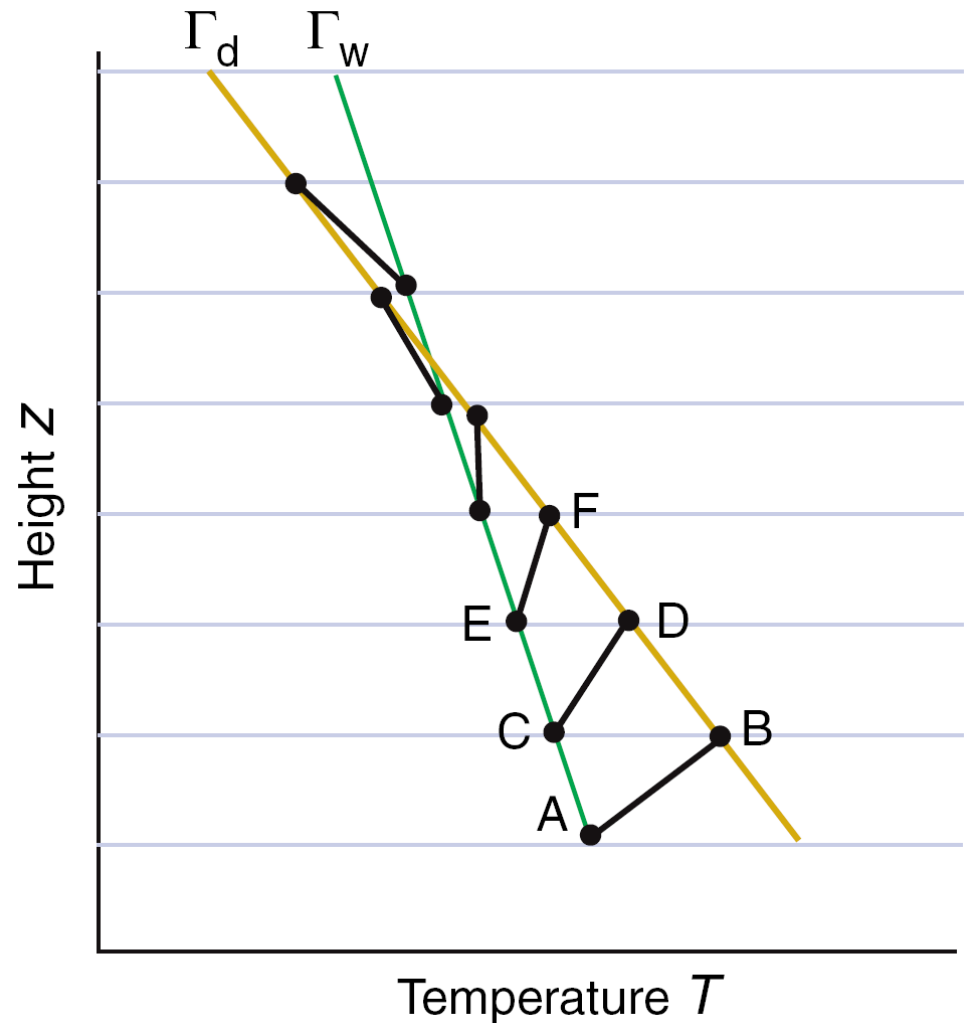
- **Substantial low-level (boundary-layer) moisture.**

- **Low-level lifting capable of releasing the instability.**

Convection-initiation environment

Convective available potential energy (**CAPE**) and convective inhibition (**CIN**)

Increase of $-dT/dz$ in lifted inversion

Realistic soundings preceding convective initiation
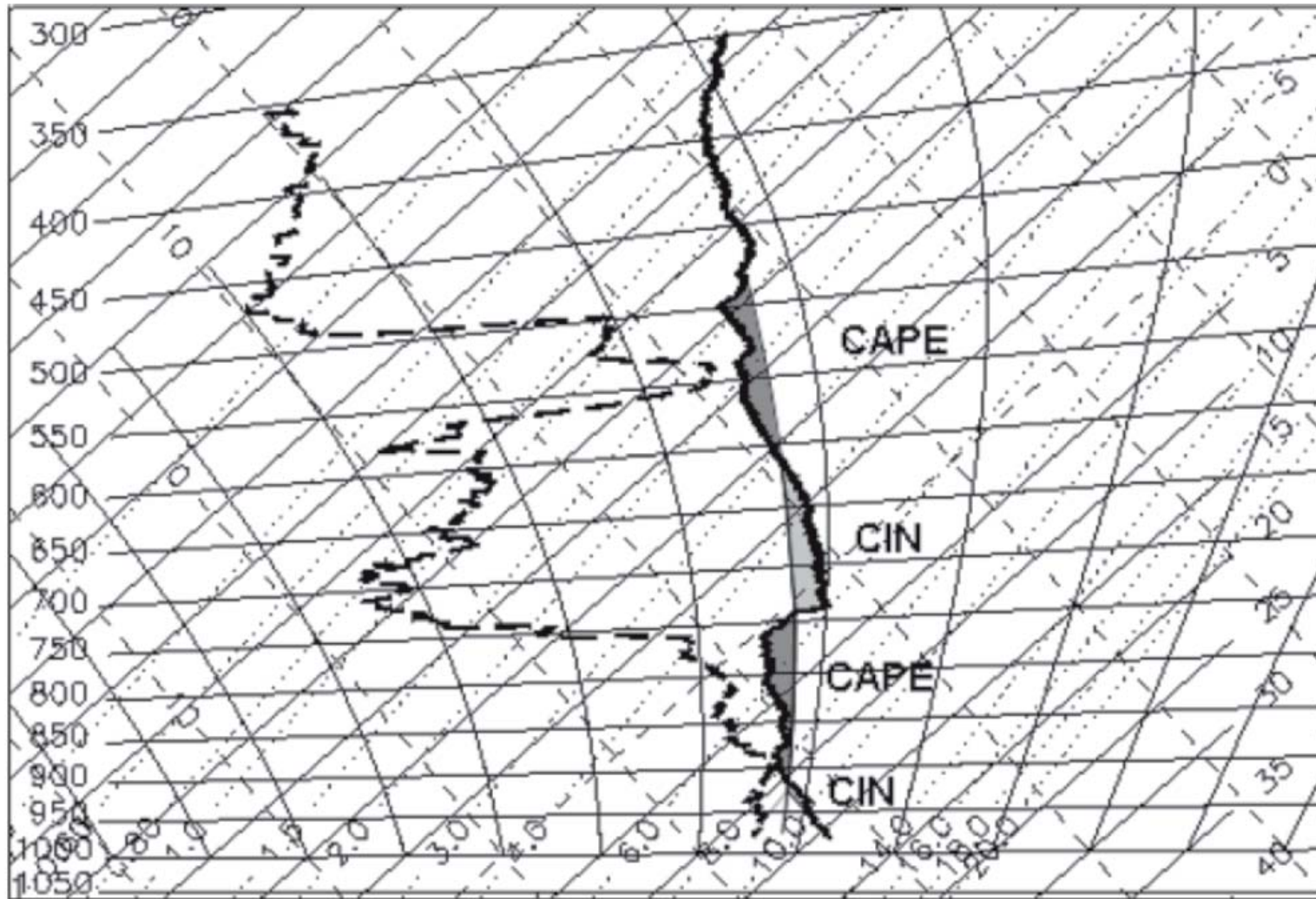
Browning et al. (2007)

FIG. 1. Tephigram for radiosonde launched from Bath at 1100 UTC on 15 Jun 2005 (IOP 1). The CAPE and CIN are shaded dark and light gray, respectively; the thin solid line partially bounding these areas is the 14°C saturated adiabat representing a parcel that ascends unmixed from the boundary layer.

Only small lift is sometimes needed to initiate convection

Browning et al. (2007)

Original profile

Lifted by 15 hPa (~150 m)

800 hPa

CAPE

CAPE

850 hPa

← Lid

900 hPa

CIN

950 hPa

1000 hPa

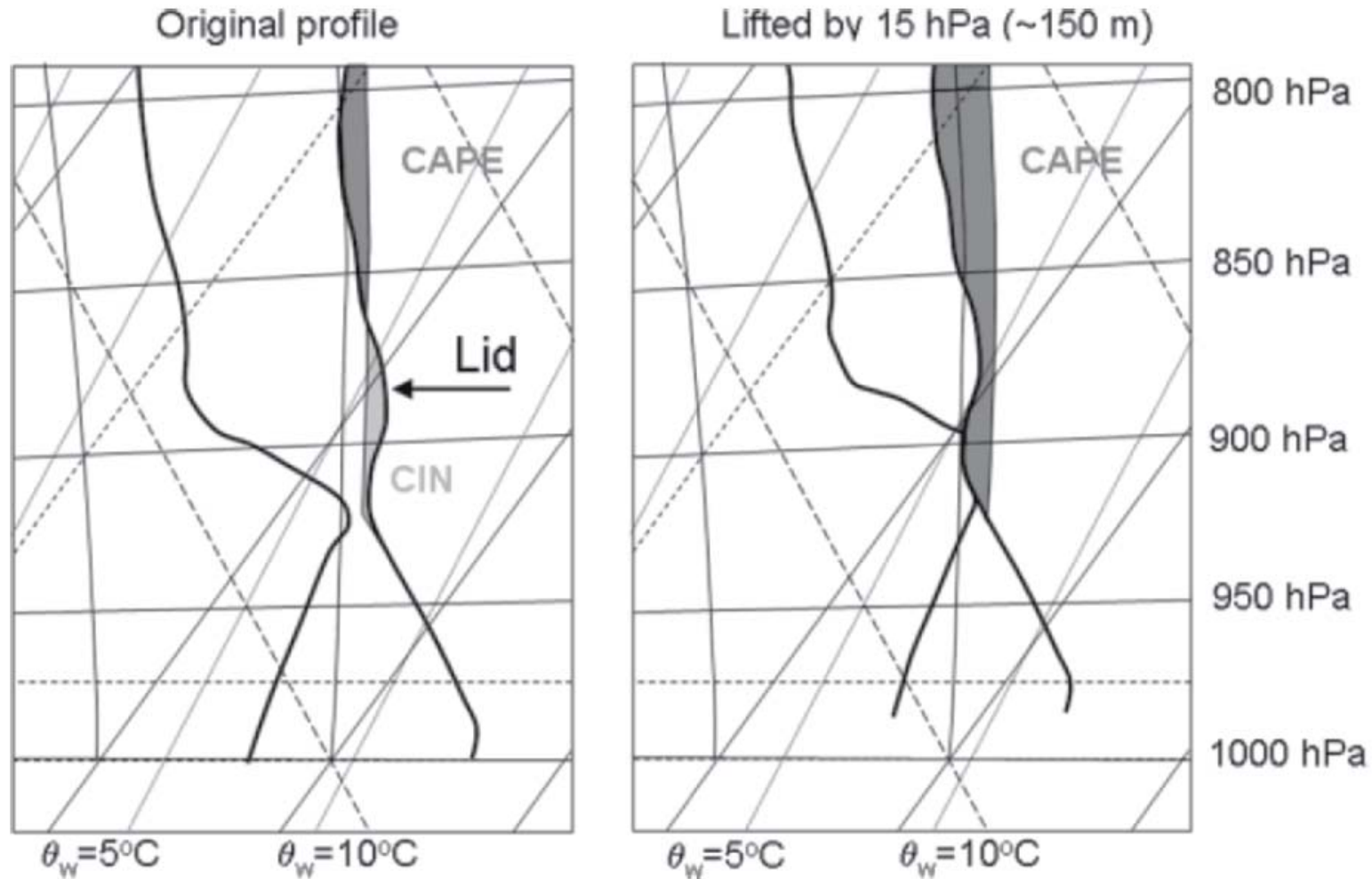$\theta_w=5°C$ $\theta_w=10°C$ $\theta_w=5°C$ $\theta_w=10°C$

FIG. 2. Illustration of how adiabatic lifting of a profile by as little as 15 hPa (~150 m) can increase the **CAPE** and completely eliminate the **CIN**. The original profile is shown on the left and the lifted profile on the right. (Adapted from Morcrette et al. 2006.)

# Mechanisms of lifting/ascent

Markowski et al. (2006)

- **Convergence along mesoscale boundaries**
  - fronts
  - drylines
  - outflow boundaries
  - sea/land breezes

- **Differential heating**
  - cloudy-clear air boundaries
  - heating of sloped terrain
  - spatial variability of buoyancy flux

- **Gravity waves and bores**

Example of convergence boundary

Browning et al. (2007)

Convective Storm Initiation Project (CSIP), UK 2004/05

MEVI 12:00Z 15/06/2005
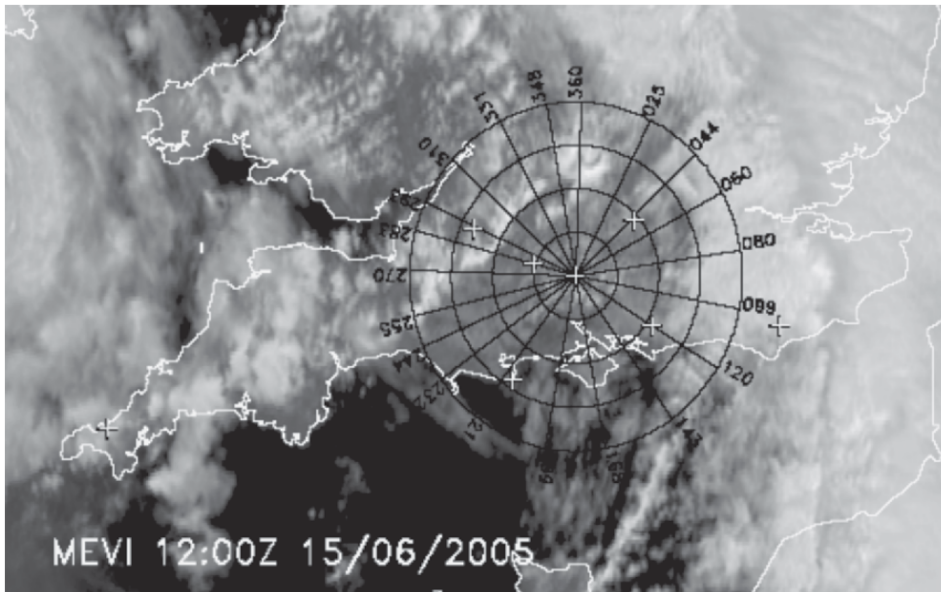
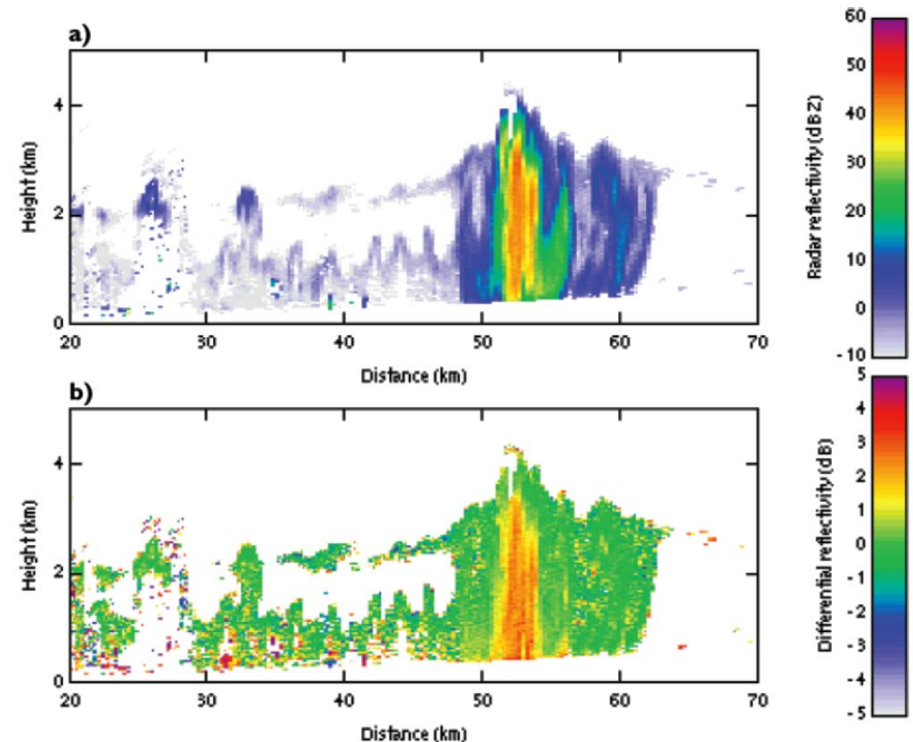**Satellite image of clouds along a convergence line**

FIG. 11. RHIs of (a) reflectivity (dBZ) and (b) differential reflectivity (dB) for a scan across the convergence line in Fig. 10, obtained from the 3-GHz Chilbolton radar at 1200 UTC 15 Jun 2005 (IOP 1).

Formation of cloud streets along a boundary layer convergence line parallel to strong low-level wind and convective rolls

Mesoscale boundaries during IHOP_2002
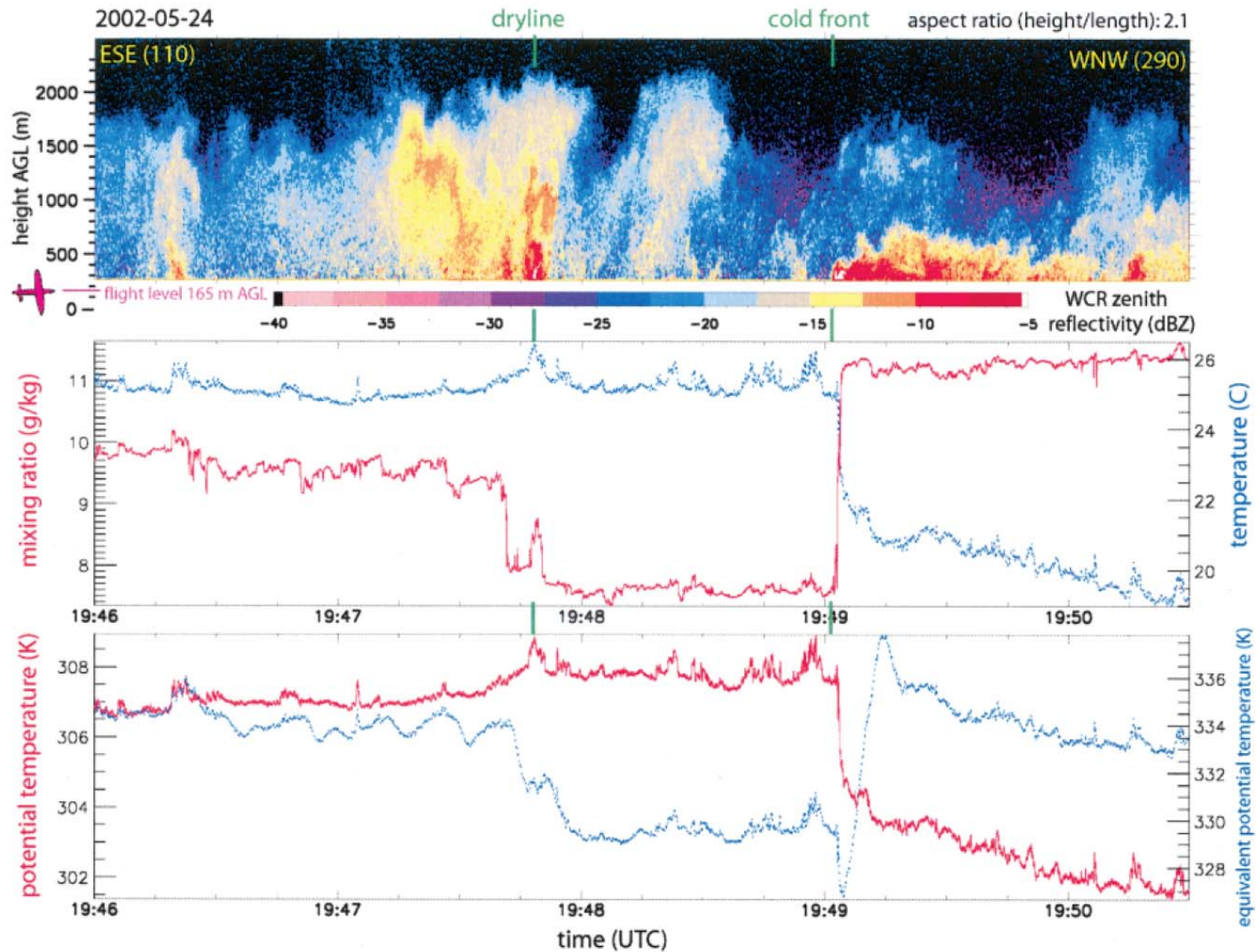
Weckwerth et al. (2004)

FIG. 8. WCR reflectivity profile above the 165-m-AGL flight level, along a 22-km-long transect from ESE to WNW on 24 May 2002 in northern Texas, showing a relatively strong, shallow (~500 m deep) cold front and a weaker but deeper dryline signature (~1800 m deep). The corresponding UWKA in situ measurements below clearly show the dryline and cold frontal signatures indicated by vertical green lines.
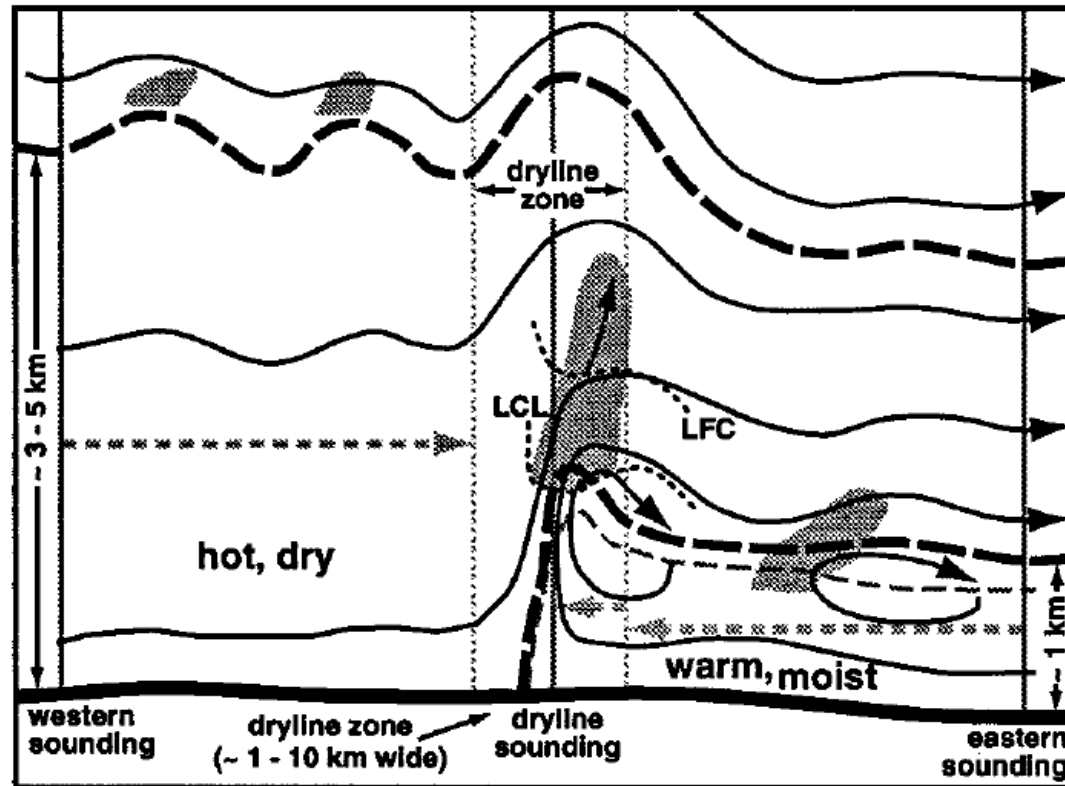
Dryline in pre-storm environment

FIG. 17. Conceptual model of dryline environment during afternoon and early evening, showing dryline position in relation to cumulus clouds and airflow streamlines. The lower heavy dashed curve denotes the extent of the moist convective boundary layer, while the upper heavy dashed curve locates the deep, dry convective boundary layer (west of dryline), and the elevated residual layer (east of dryline and above moist layer). The gray dashed curve locates the surface of zero westerly wind component. The vertical gray lines locate proximity and dryline soundings described in the text. The heavy dashed streamline denotes a buoyantly accelerated cloudy air parcel trajectory.

Ziegler and Rasmussen (1998)

Outflow and dryline on June 12, 2002, during IHOP

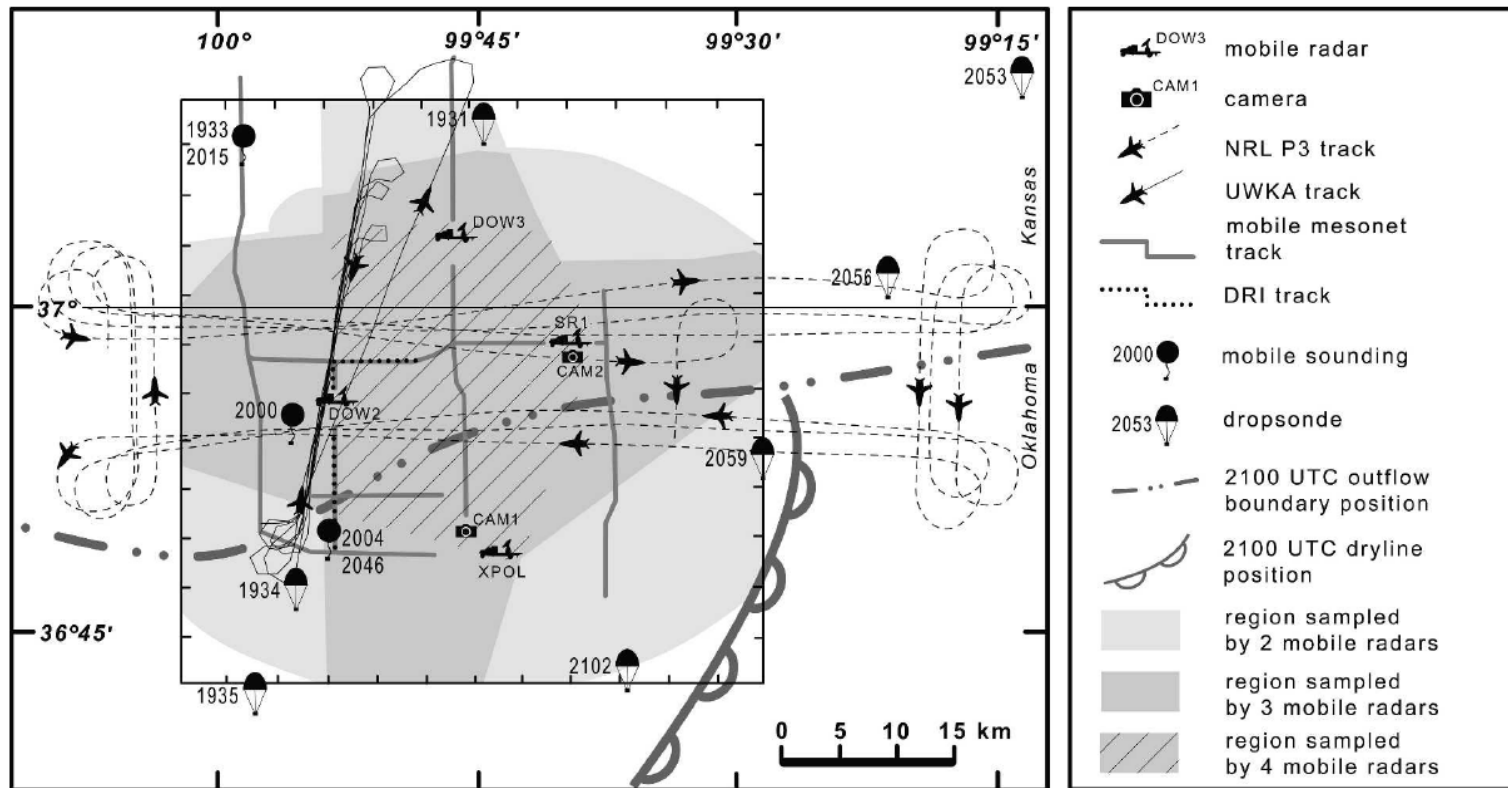**Markowski et al. (2007)**

FIG. 1. Observations obtained during the 1930–2130 UTC mobile radar deployment on 12 Jun 2002. The locations of camera, mobile mesonet, dropsonde, rawinsonde, aircraft (NRL P-3 and UWKA), mobile radar (DOW2, DOW3, XPOL, SR1), and mobile radiometer (DRI) observations are indicated using the symbology defined in the legend. The square encloses the 50 × 50 km² mobile radar analysis region (the same region indicated in Figs. 3, 4, and 6). The positions of mesoscale boundaries at 2100 UTC also are overlaid.

Surprising finding: convergence and vertical motion fields were dominated by boundary layer motions rather than by dynamics associated with the mesoscale boundaries.

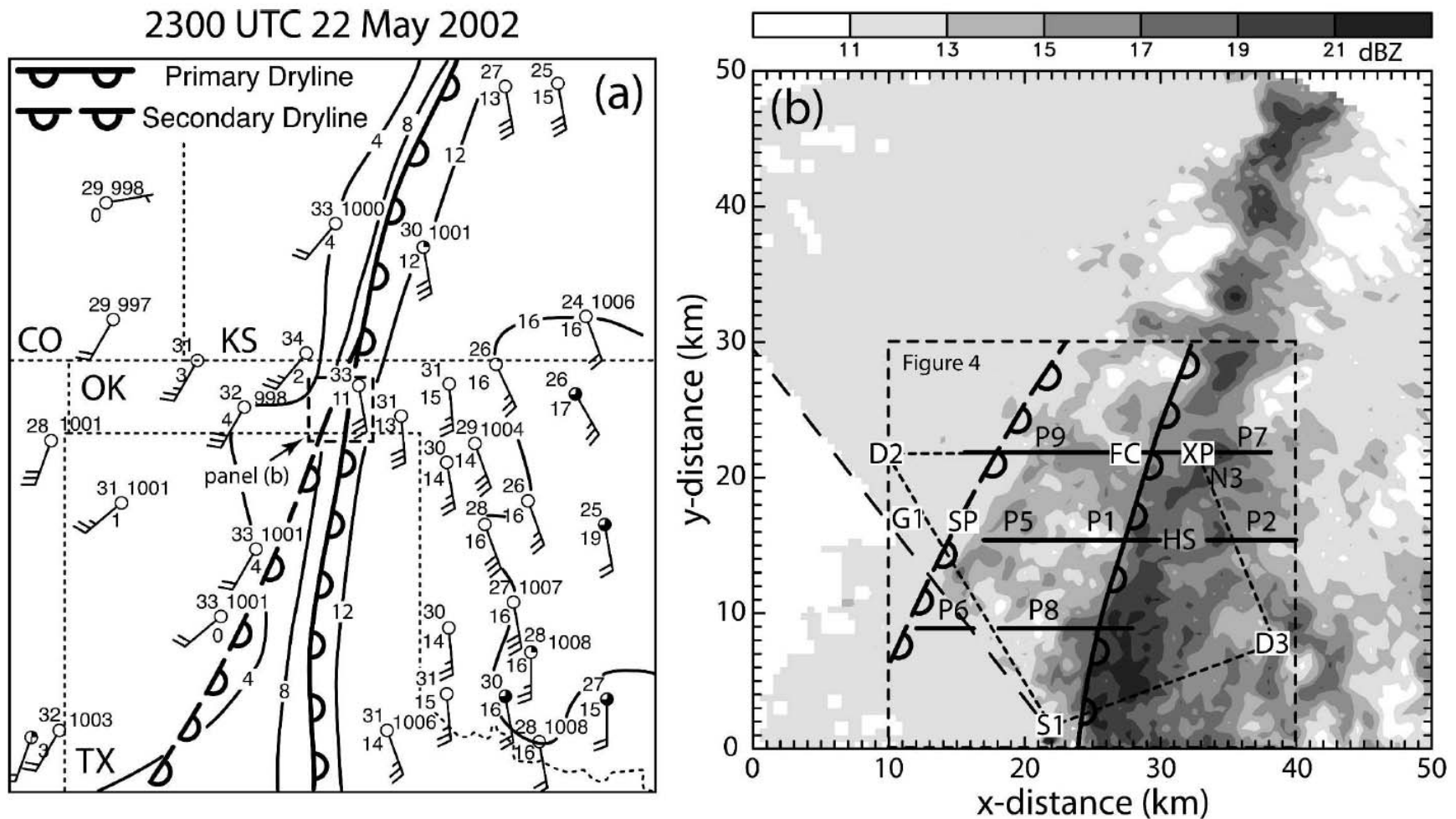# Dryline on May 22, 2002, during IHOP

Buban et al. (2007)

FIG. 1. Surface conditions at 2300 UTC 22 May 2002. (a) Surface map with standard station models and subjectively analyzed dewpoint (solid black lines, °C). (b) Radar reflectivity (dBZ) in the radar analysis domain including the locations of the radars and mobile mesonet legs. The location of the radar analysis domain is shown by the dashed box in (a). The black dashed box in (b) is the thermodynamic analysis domain. The long dashed line indicates the edge of SR1 data. In both panels, the locations of the primary dryline (solid line with semicircles) and the minor dryline (dashed line with semicircles) are shown. Platform abbreviations are as follows: Field Coordination vehicle (FC), Probe 1, 2, . . . (P1, P2, . . .), DOW2 (D2), DOW3 (D3), X-Pol (XP), S-Pol (SP), SMART radar (S1), mobile CLASS (N3), mobile GLASS (G1), and Homestead location (HS).

Key question:
How do mesoscale forcing and boundary-layer-scale processes interplay in the development of deep convection?

Role of low-level (boundary-layer) shear

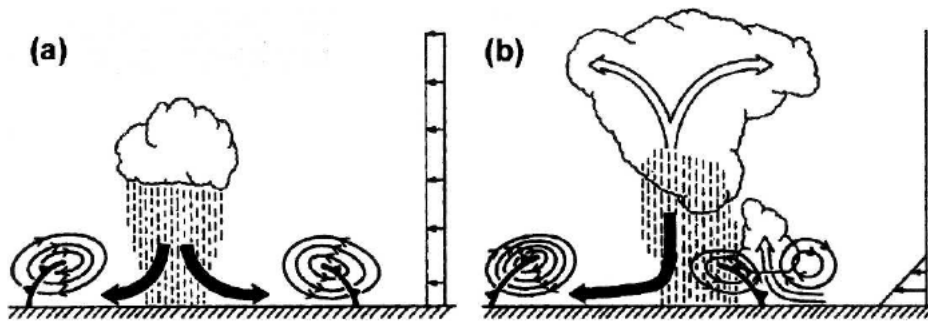**Weckwerth and Parsons (2006)**

(a) (b)

FIG. 2. Conceptual model of importance of low-level shear in the evolution of convection. (a) Without low-level shear, the cold-pool circulation inhibits deep vertical lifting and inhibits new convection. (b) With low-level shear countering the cold-pool circulation, new cells can be triggered. (From Rotunno et al. 1988.)

Convection inhibition without shear (a)

Convection promotion with shear (b)

FAVORABLE FOR STORMS

UNFAVORABLE FOR STORMS
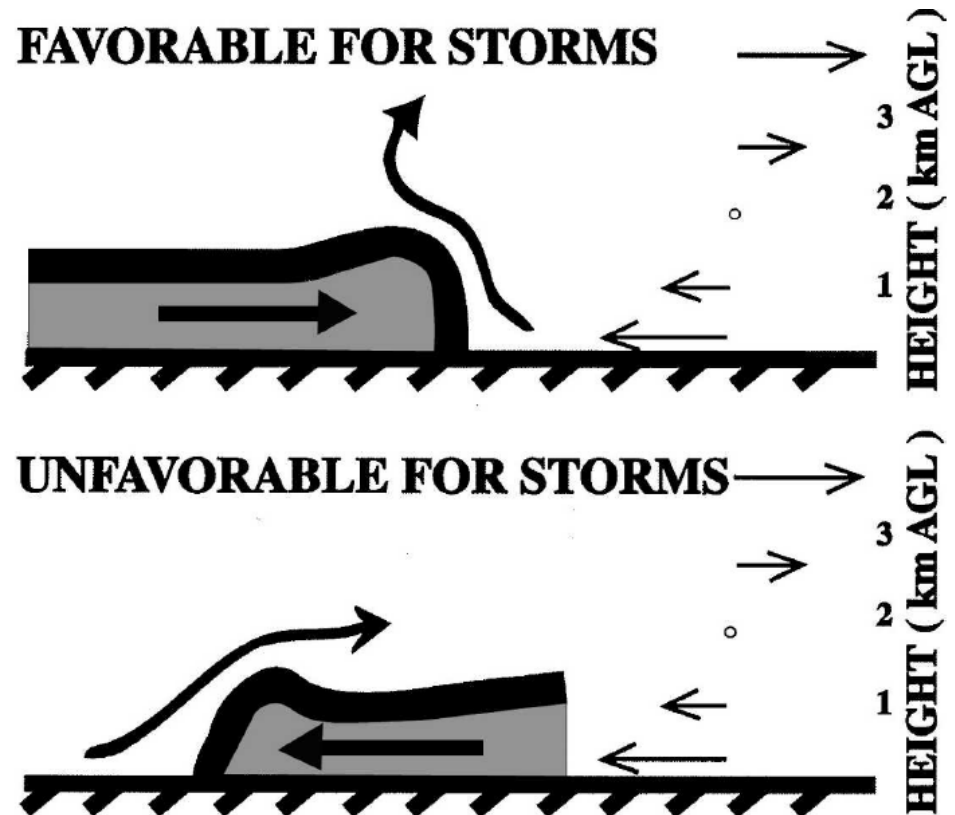
FIG. 3. Schematic illustration of dynamic conditions (top) favorable and (bottom) unfavorable for CI derived from observations in a relatively low shear environment. The wind vectors on the right represent the environmental wind profile, which is the same for both cases. The dark shading represents a density current, or boundary. The curved arrow ahead of the density current represents the updraft tilt. (From Wilson et al. 1998.)

Vorticity of updraft enhanced through ingesting boundary layer vorticity

Wallace and Hobbs (2005)
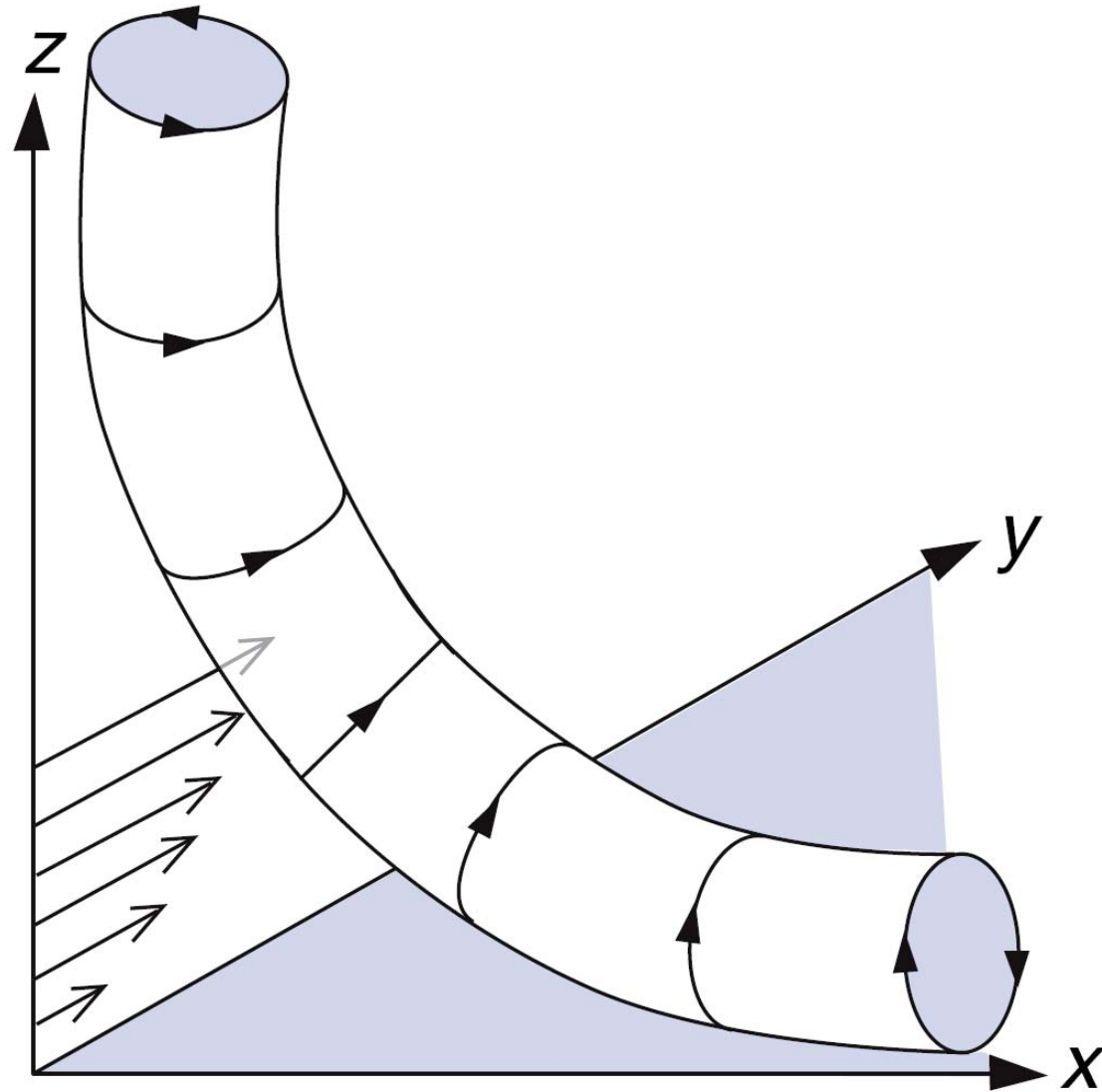
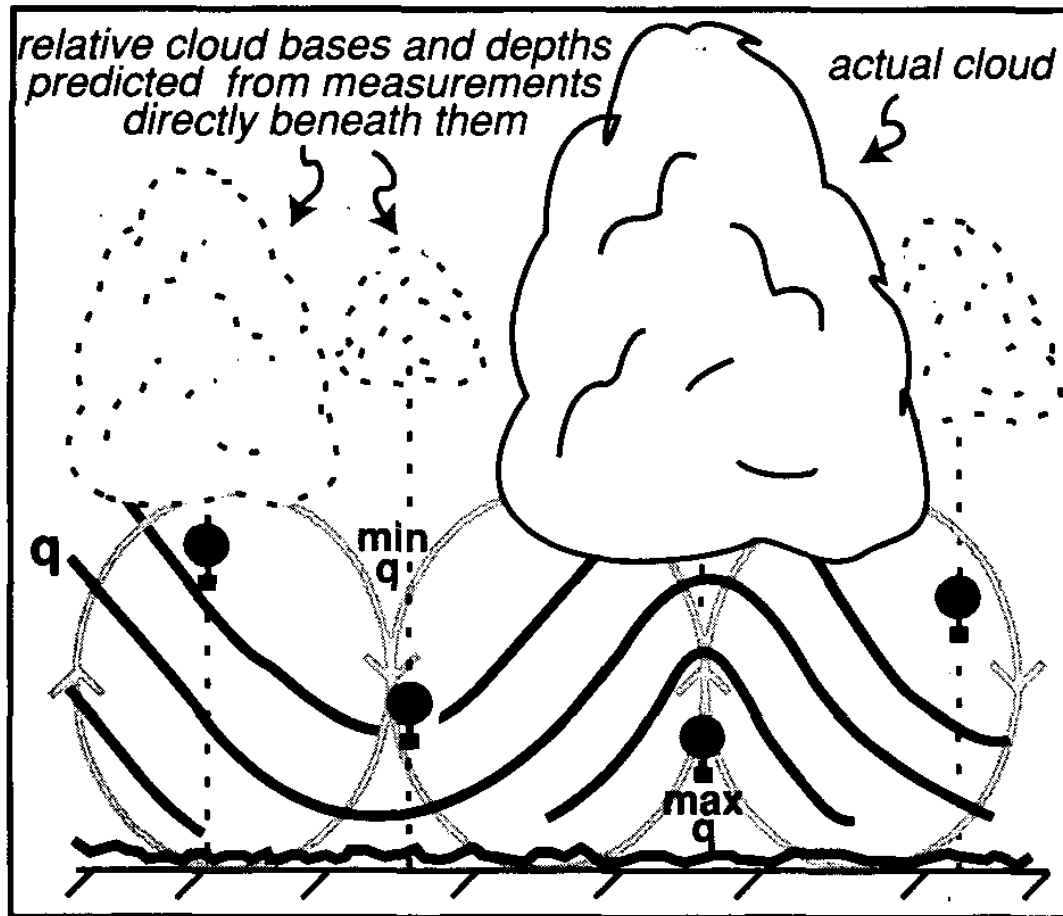# CBL variability associated with convective rolls

FIG. 10. Schematic diagram summarizing results of this study. Gray lines indicate roll circulations. Thick black lines are contours of moisture with the maxima existing within the roll updraft regions. Actual cloud base and depth are shown by the solid cloud. Dashed clouds represent relative cloud bases and depths expected if stability parameters were estimated from CBL moisture values directly beneath those clouds.

Weckwerth et al. (1996)

Satellite and radar images of convective rolls
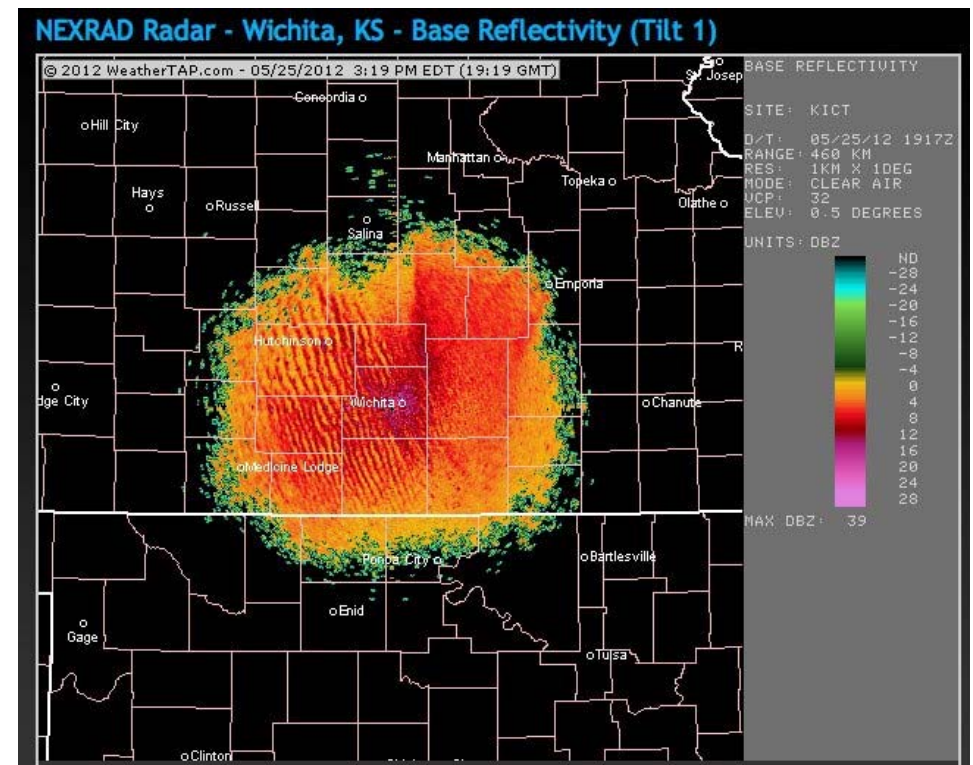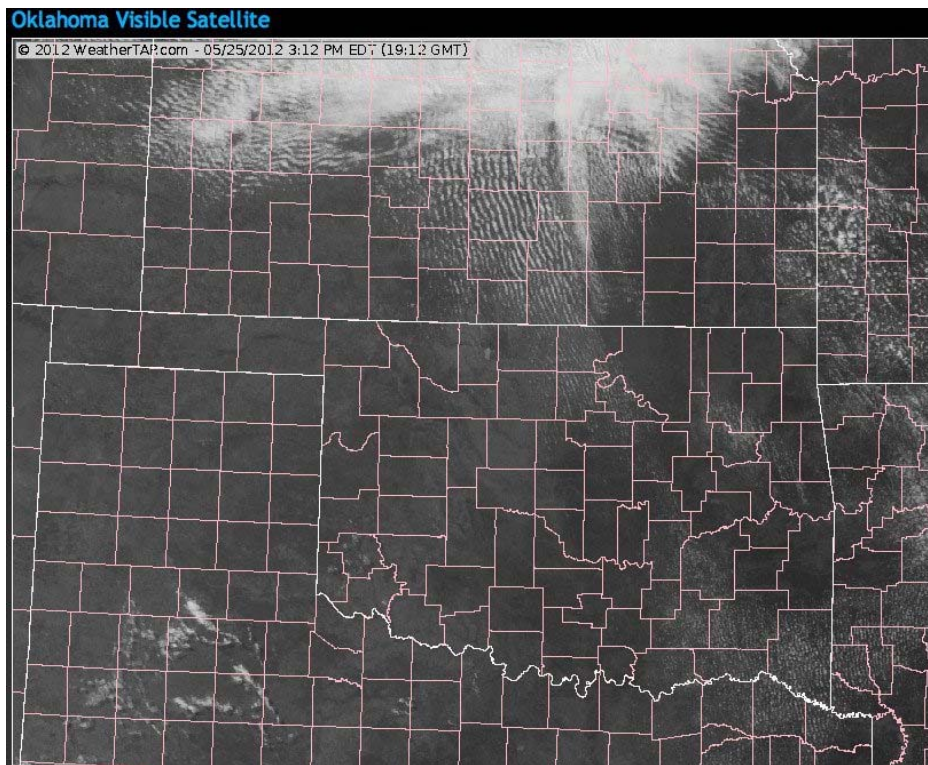
Radar observations of IHOP's May 22, 2002, dryline

Buban et al. (2007)
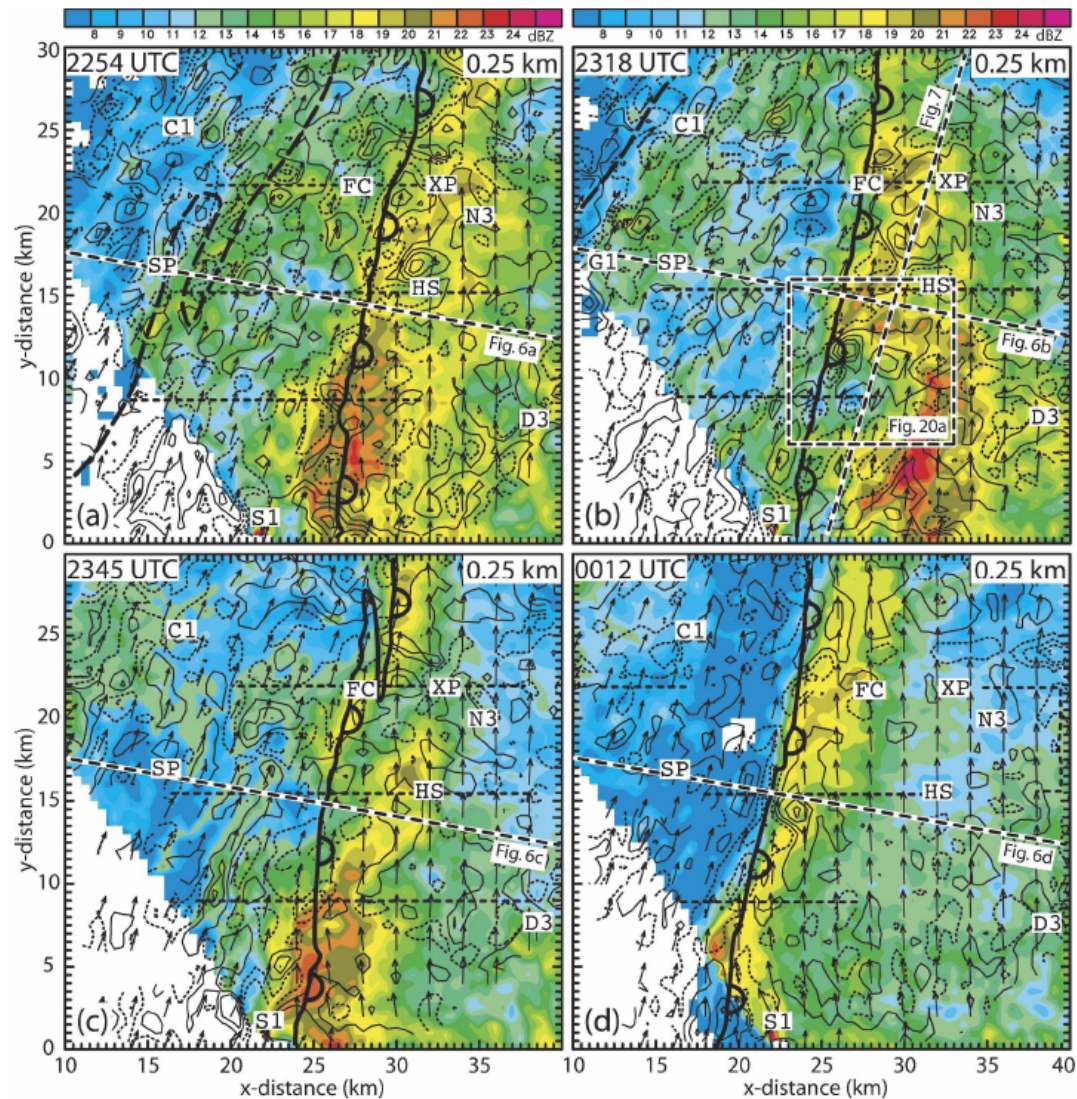
FIG. 4. Radar analysis fields at 0.25 km AGL at (a) 2254, (b) 2318, (c) 2345, (d) 0012 UTC 22 May 2002. Reflectivity (dBZ), horizontal wind vectors (every fourth grid point with 1-km vector length equal to 15 m s⁻¹), and vertical vorticity (s⁻¹) every 2 × 10⁻³ s⁻¹ with positive values (black solid lines) starting at 1 × 10⁻³ s⁻¹ and negative values (black dotted line) starting at −1 × 10⁻³ s⁻¹. Also labeled are the locations of the Field Coordinator vehicle (FC), the digital camera (C1), the mobile GLASS (G1), and CLASS (N3) sounding systems, DOW3 (D3), X-Pol (XP), the SMART radar (SR1), and Homestead (HS). The thin dashed lines locate the mobile mesonet legs. The thick dashed black lines indicate the locations of cross sections shown in Figs. 6, 7, and 21. The positions of the primary (thick scalloped curve) and minor (thick dashed curve) drylines as determined by the thermodynamic analyses are also shown as in Fig. 1, including the 2251 UTC dryline positions in (a).

BL flow structure in dryline-normal direction (IHOP, May 22)
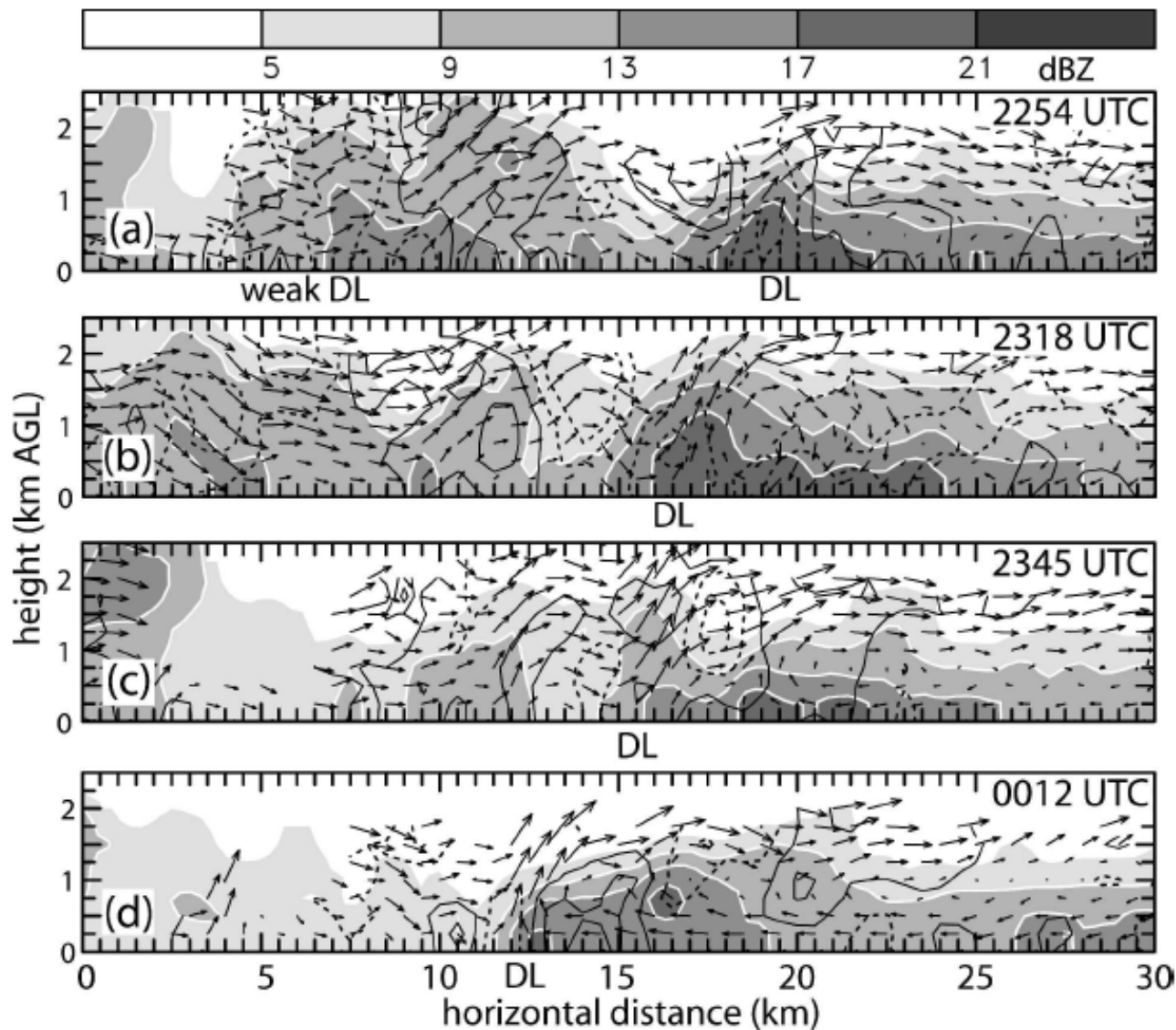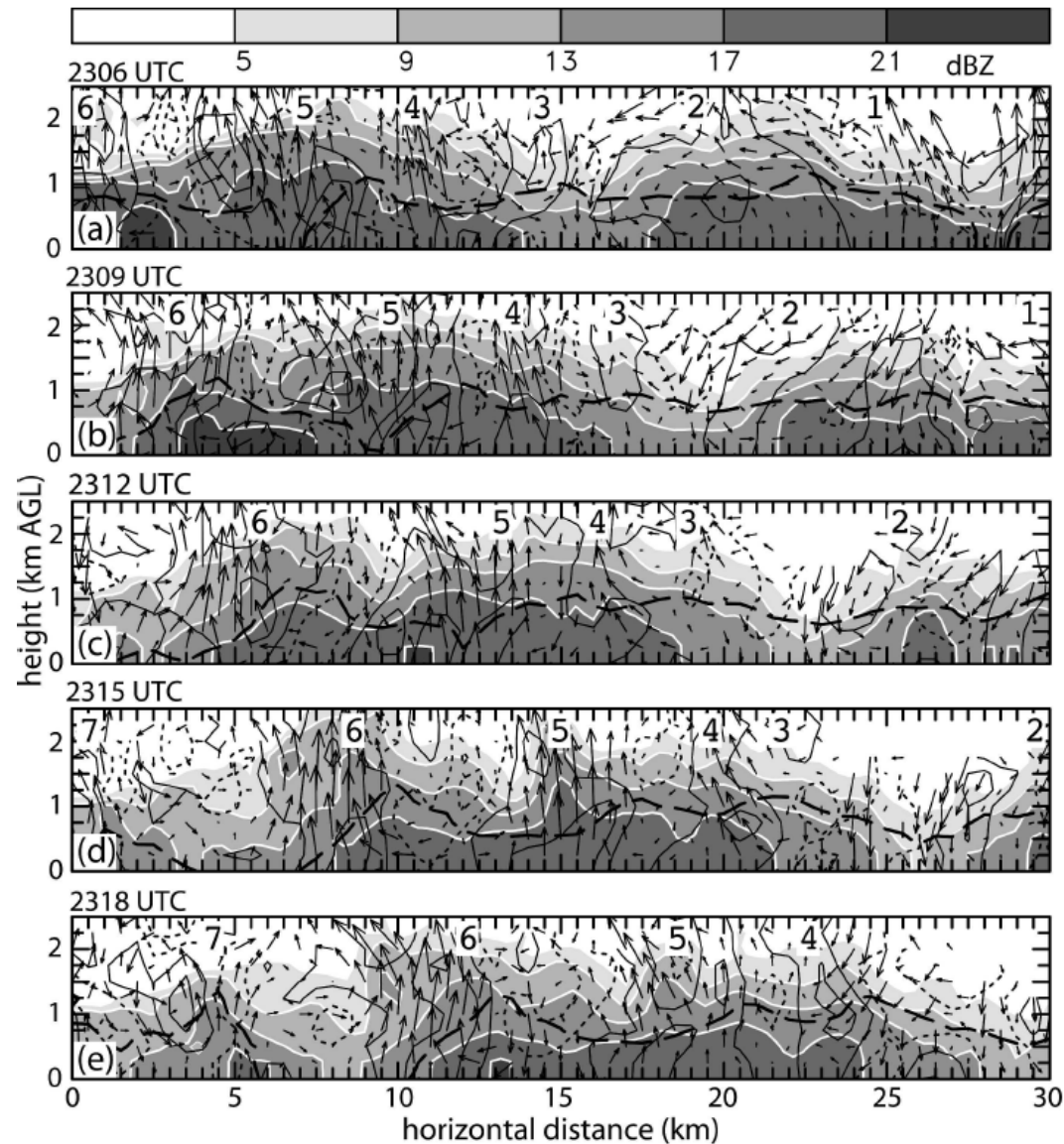
Buban et al. (2007)

FIG. 6. Vertical dryline-normal cross sections of reflectivity (dBZ), ground-relative wind vectors with 1-km length equal to 10 m s^{-1}, and vertical vorticity (s^{-1}, every 2×10^{-3} s^{-1}) with positive values (black solid lines) starting at 2×10^{-3} s^{-1} and negative values (black dotted line) starting at -2×10^{-3} s^{-1}. Cross section locations are indicated in Fig. 4.

BL flow structure in dryline-parallel direction (IHOP, May 22)

Buban et al. (2007)

FIG. 7. Vertical dryline-parallel cross sections of reflectivity (dBZ), misocyclone-relative wind vectors (1-km length equal to 5 m s^{-1}), and vertical vorticity (s^{-1}) every 2×10^{-3} s^{-1} with positive values (black solid lines) starting at 2×10^{-3} s^{-1} and negative values (black dotted line) starting at -2×10^{-3} s^{-1}. Above (below) the long dashed black line, the flow is greater than (less than) zero out of (into) the plane. A constant reference horizontal wind, from 194° at 20.6 m s^{-1}, was subtracted from the wind vectors to better identify circulations. Cross section locations are indicated in Fig. 4. Individual transverse rolls are numbered in order of appearance.

Conceptual view of flow interactions in dryline environment

Buban et al. (2007)
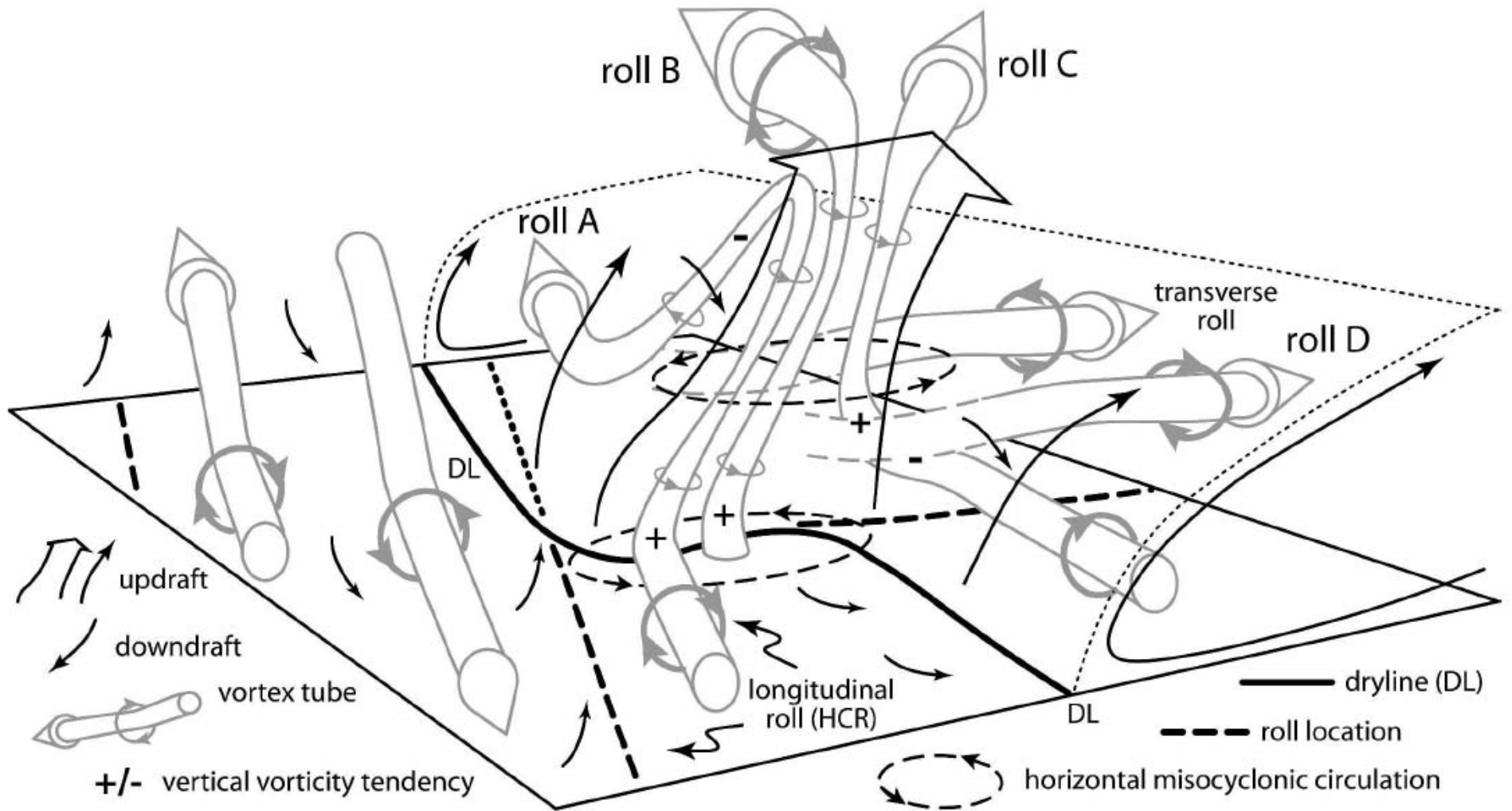
FIG. 22. Conceptual model of misocyclones embedded within the dryline on 22 May 2002. Vortex tubes associated with HCRs, transverse rolls, the dryline, and the misocyclone are shown in gray. The heavy solid line denotes the dryline location and the thin dotted black line indicates the moist layer.

Characterizing sheared CBL flow structure

Shear vs. buoyancy forcing in the surface layer (Lecture II):

$$\zeta = z/L, \text{ where } L = -\frac{(-\overline{u'w'})^{3/2}}{\kappa \overline{w'b'}} = \frac{u_*^2}{\kappa b_*} \text{ is the M-O length.}$$

Shear vs. buoyancy forcing in the CBL:

$$-z_i/L, \text{ where } z_i \text{ is the CBL depth scale (inversion height).}$$

Can also be expressed in terms of ratio of two velocity scales:

$$-z_i/L = \kappa \left(\frac{w_*}{u_*}\right)^3, \text{ where } w_* = (z_i \overline{w'b'})^{1/3}, \ u_* = (-\overline{u'w'})^{1/2}.$$

Large $-z_i/L \longrightarrow$ **dominance of buoyantly produced turbulence organized in cells on large scales.**

Small $-z_i/L \longrightarrow$ **dominance of mechanically produced turbulence organized in rolls on large scales.**

Wind tunnel model of sheared atmospheric CBL

Experimental setup in the thermally stratified wind tunnel of KIT
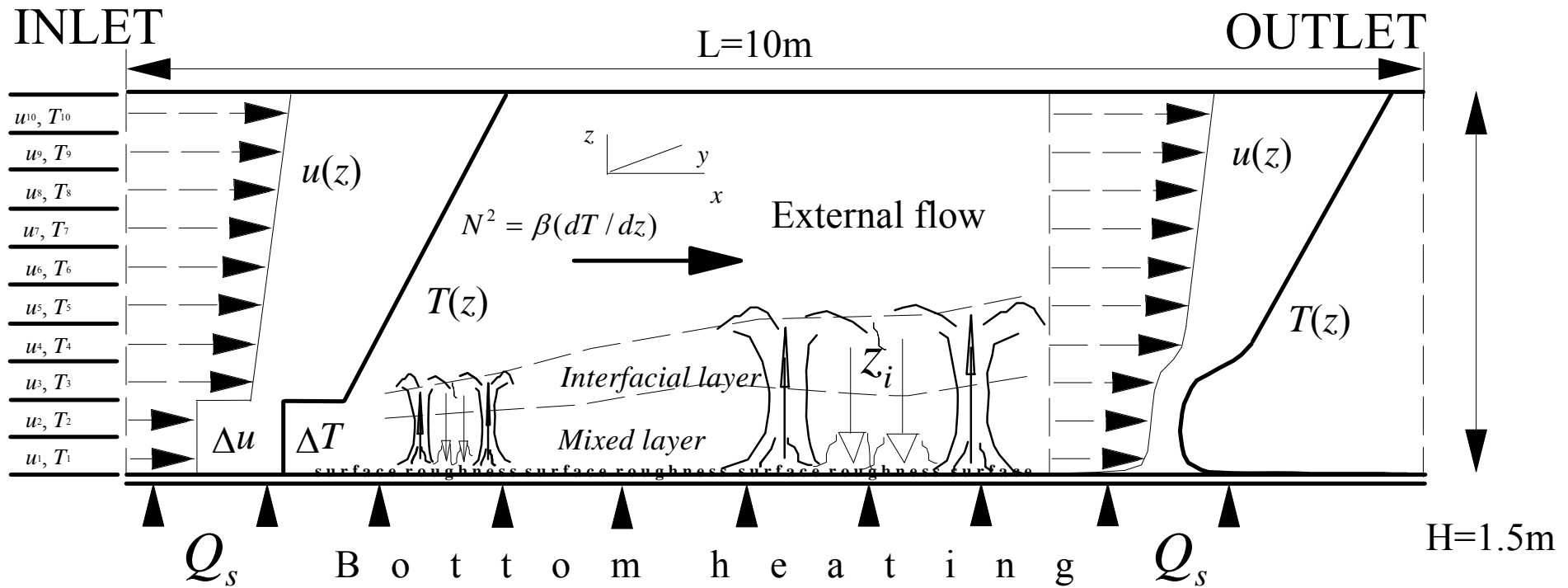
Richardson numbers: $\mathrm{Ri}_{\Delta T} = \beta w_*^{-2} z_i \Delta T$ and $\mathrm{Ri}_N = N^2 z_i^2 w_*^{-2}$

Shear/buoyancy forcing ratio: u_* / w_*, where $w_* = (\beta Q_s z_i)^{1/3}$

Atmospheric CBL:	$\mathrm{Ri}_{\Delta T} < 100$	$\mathrm{Ri}_N < 100$	$u_* / w_* < 1$
UniKA wind tunnel:	$\mathrm{Ri}_{\Delta T} < 10$	$\mathrm{Ri}_N < 20$	$u_* / w_* \approx 0.3$
Water tank, D-W:	$\mathrm{Ri}_{\Delta T} = 15$	$\mathrm{Ri}_N = 100$	$u_* / w_* = 0$ **(shear-free CBL)**

Thermally stratified wind tunnel of KIT

Interior of the tunnel

Exterior of the tunnel

Visualized CBL flow
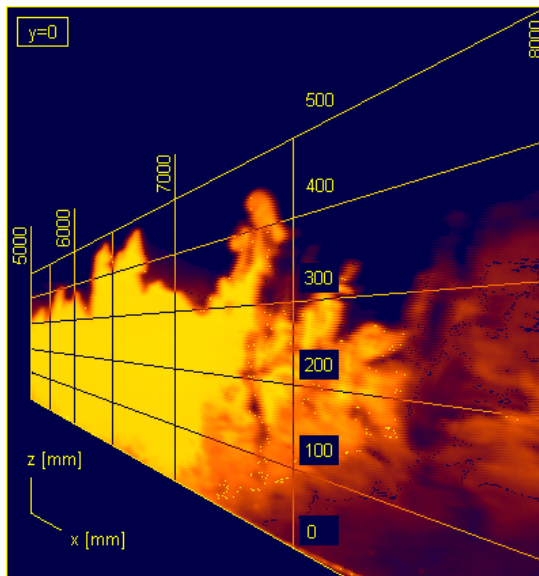
Visualized neutral BL flow
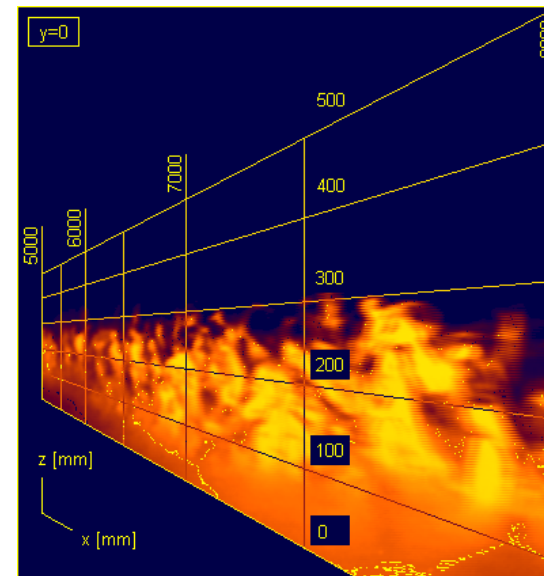
Entrainment in the horizontally evolving CBL

LES, instanteneous T
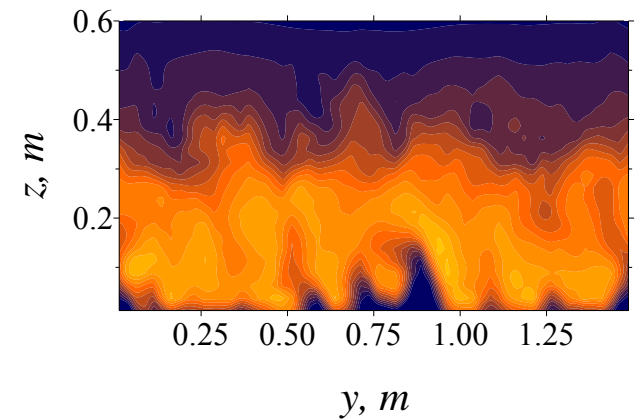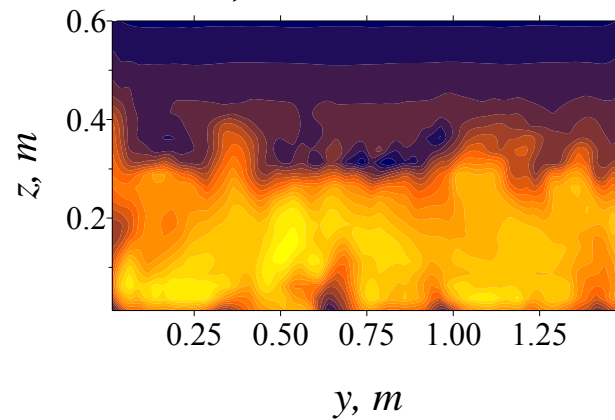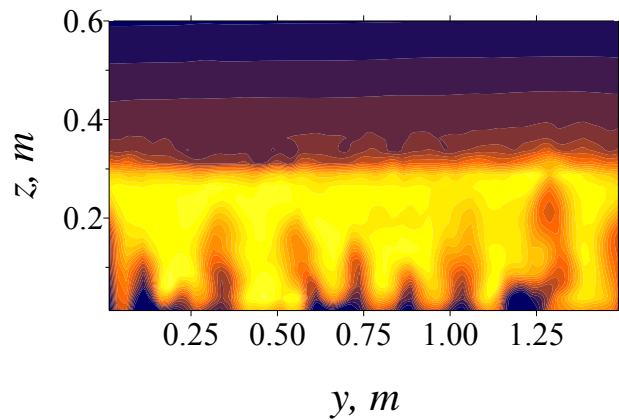
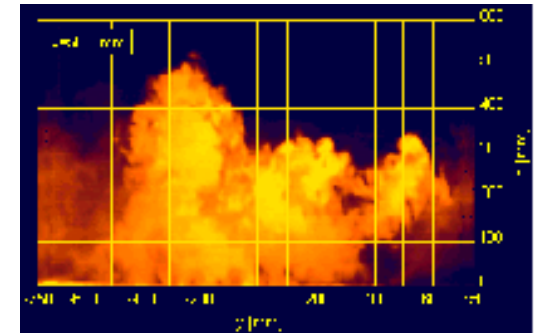## Visualization in the wind tunnel
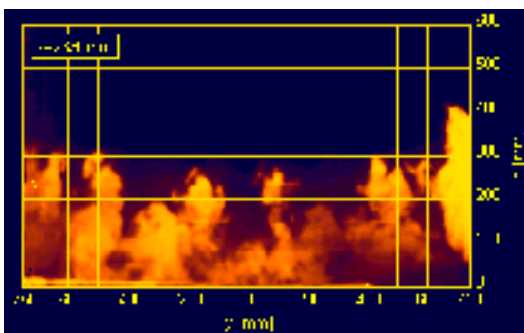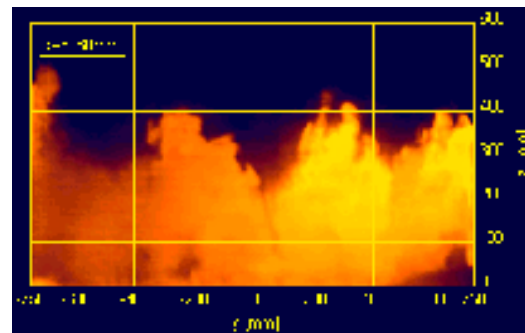
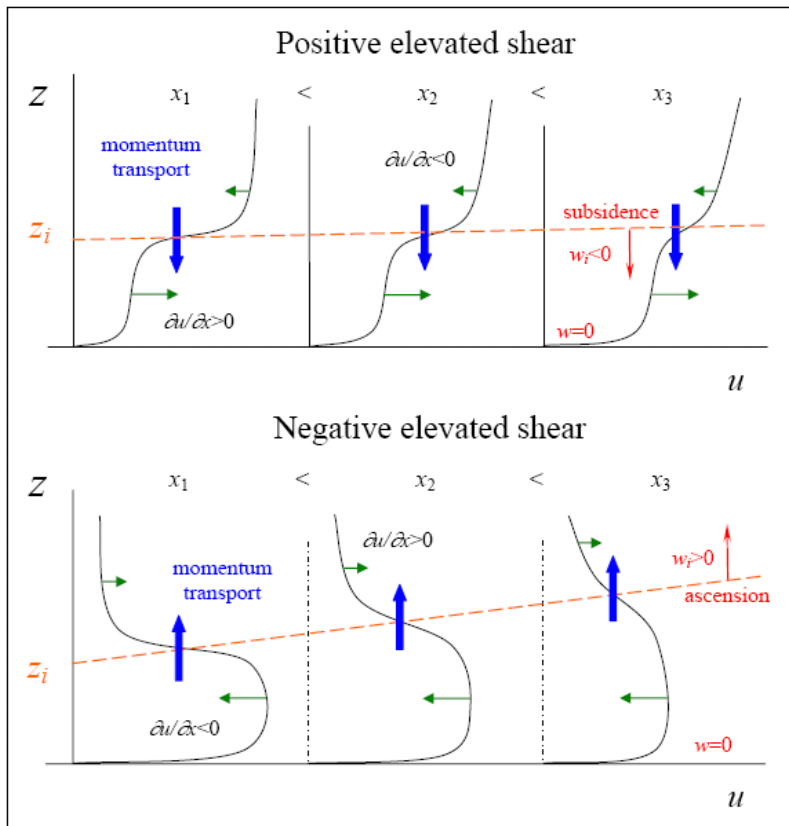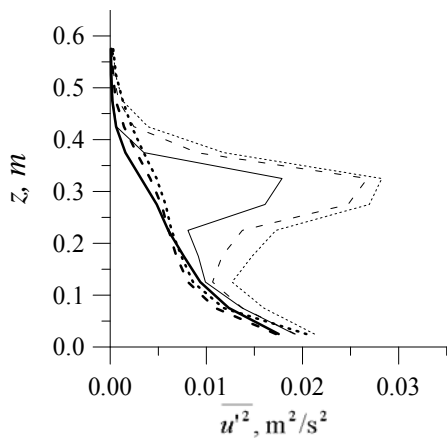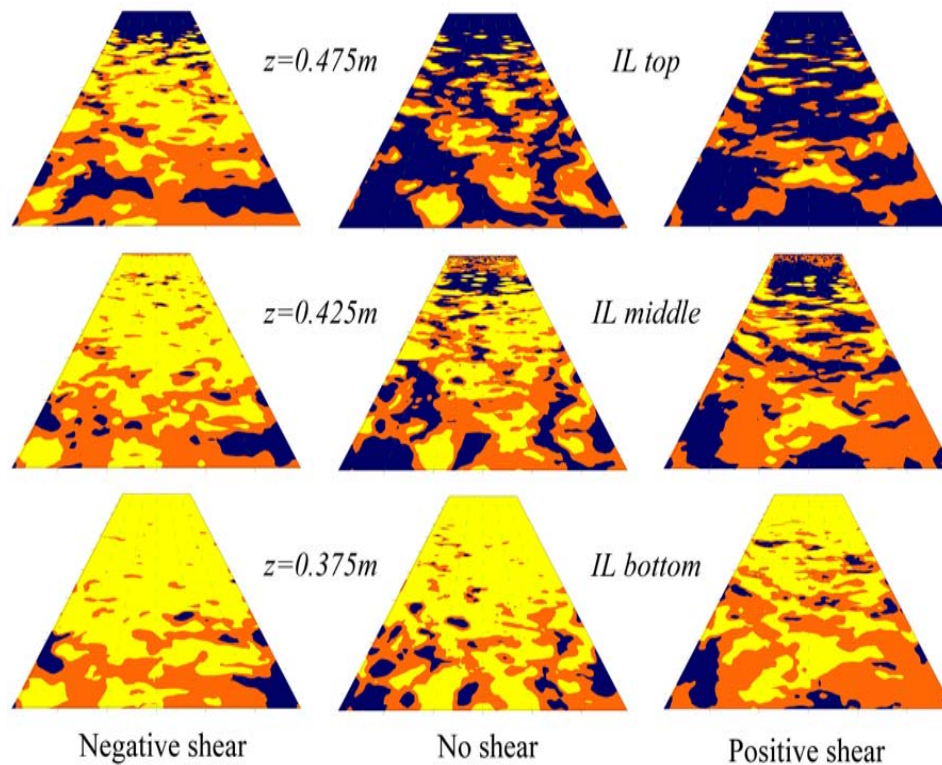x=2.33m   x=3.98m   x=5.63m
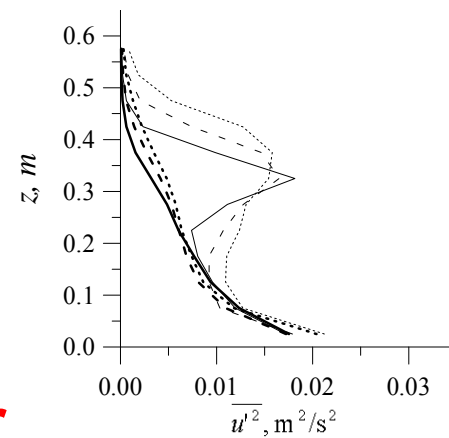
Shear versus entrainment in control of the CBL growth

Positive shear

Negative shear

Simulated sheared vs. shear-free CBL structure

OU-LES (free)   WRF-LES (free)

w at z/z_i=0.25

OU-LES (shear)   WRF-LES (shear)
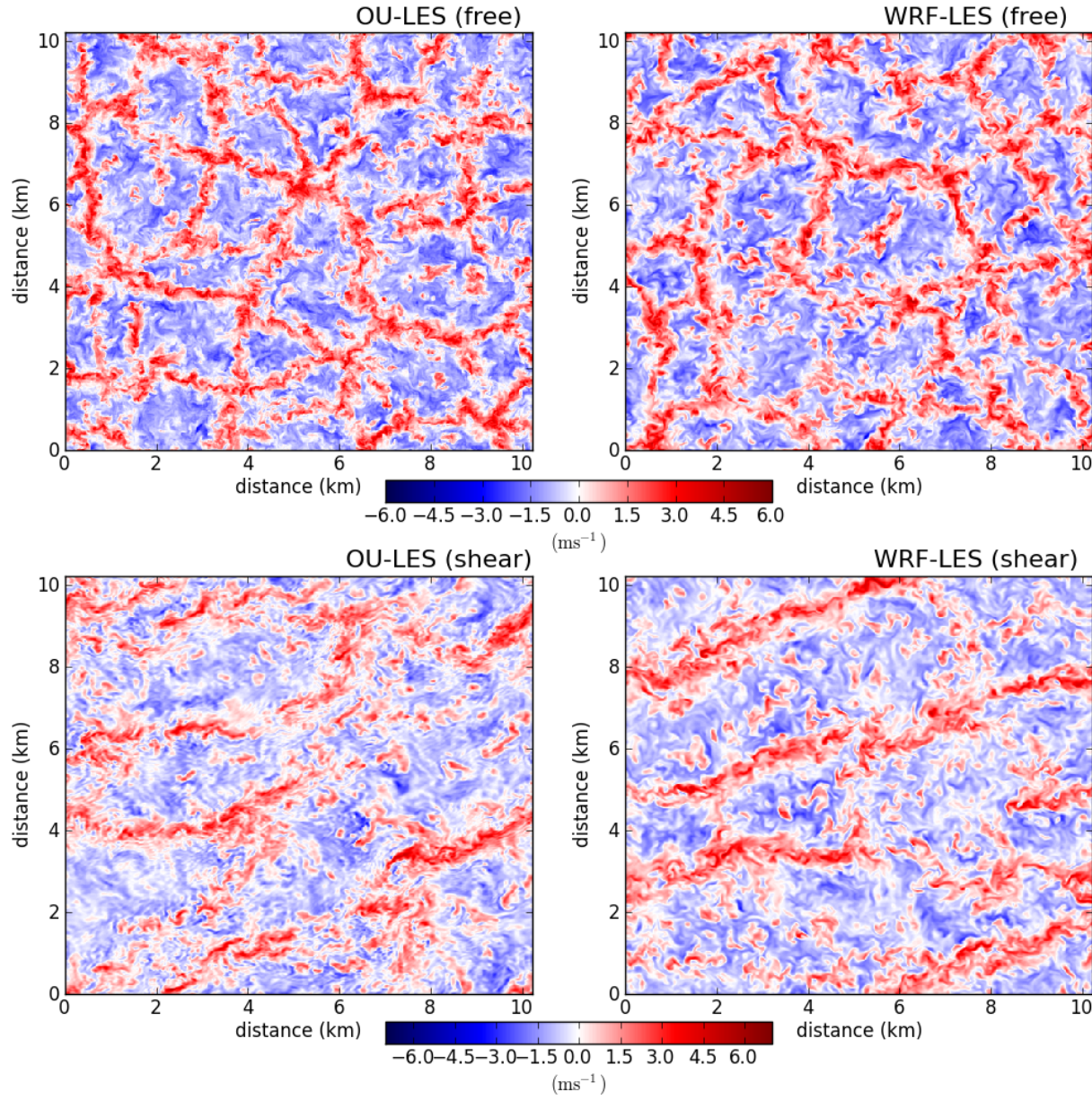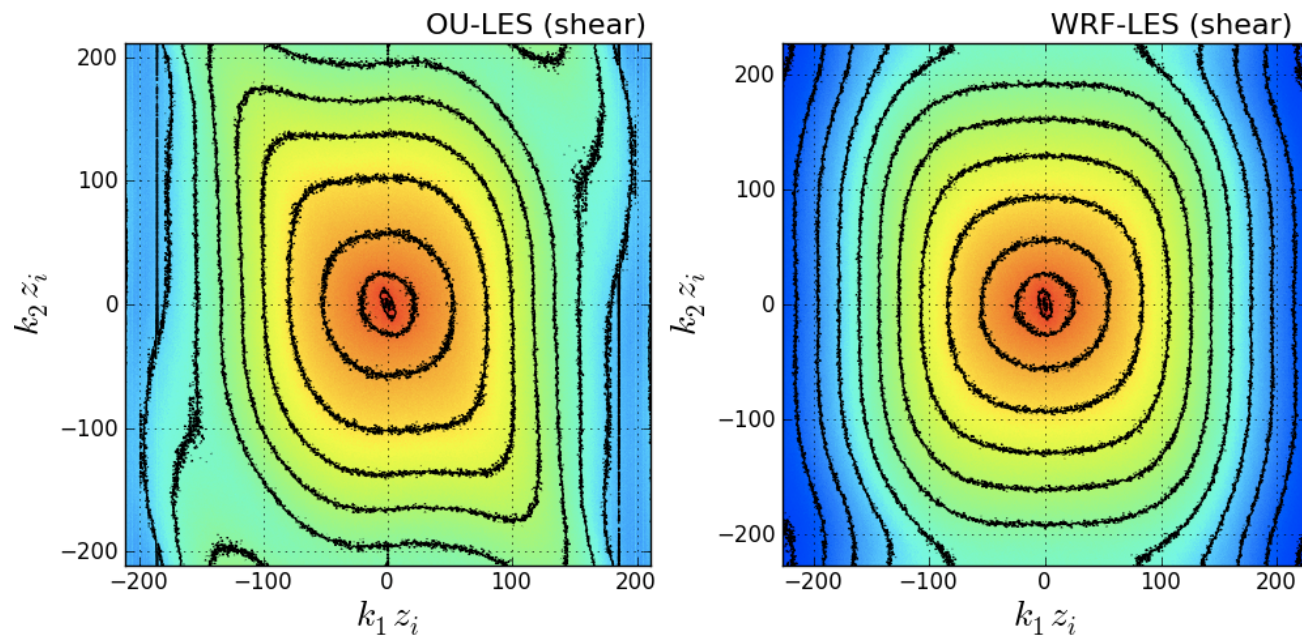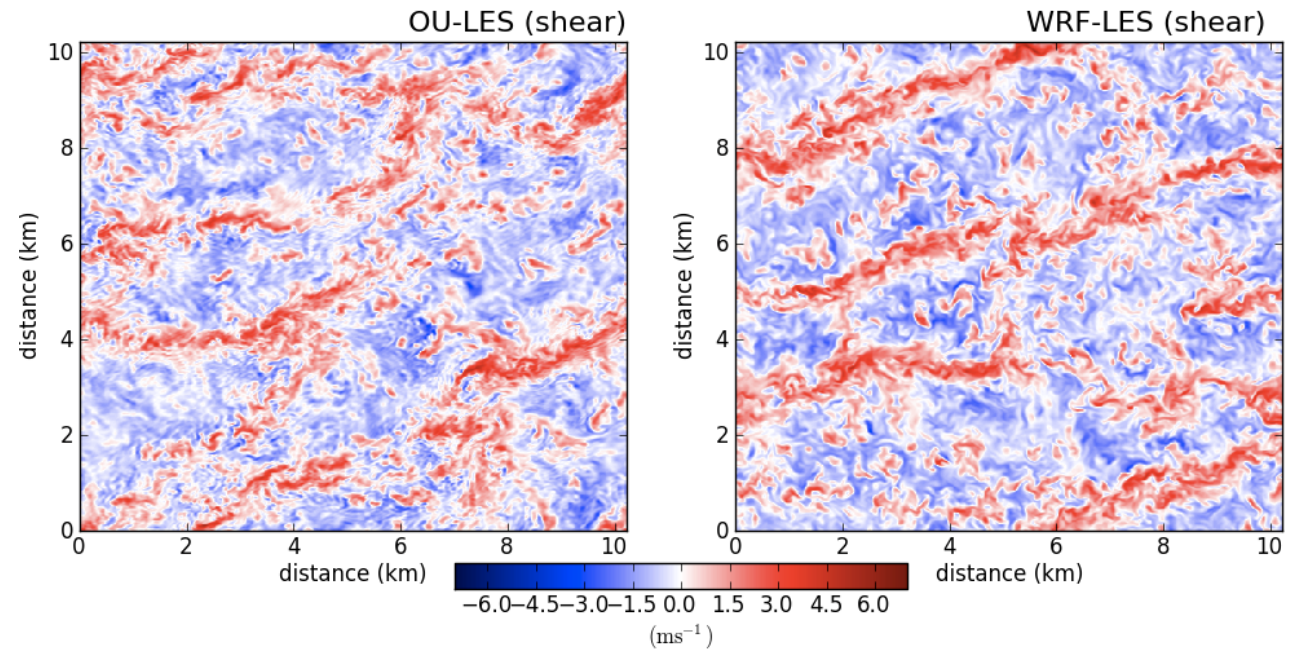
z_i/L=8 z_i/L=11

Structure of CBL revealed by planar spectra of w

Structure of sheared CBL in vicinity of dryline: I

Conzemius and Fedorovich, MWR (2008)
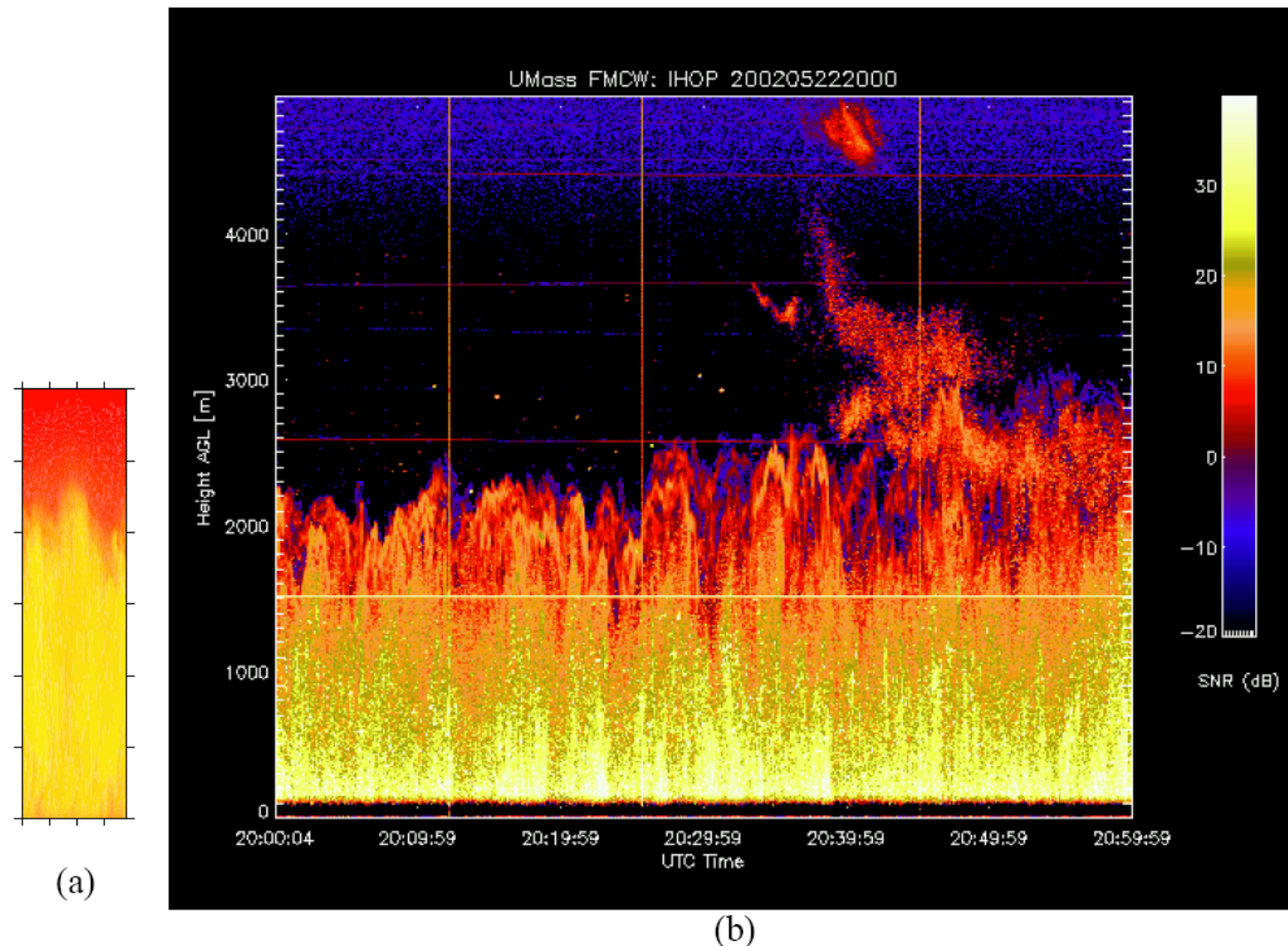

FIG. 12. CBL cross sections at concurrent times during the simulation and observations: (a) virtual potential temperature y–z cross section from the simulation at 1950 UTC (see Fig. 11), with its aspect ratio changed to match that of (b) the time–height cross section of signal to noise ratio (dB) from the University of Massachusetts FM-CW S-band radar from approximately 1900 to 2000 UTC.

Structure of sheared CBL in vicinity of dryline: II
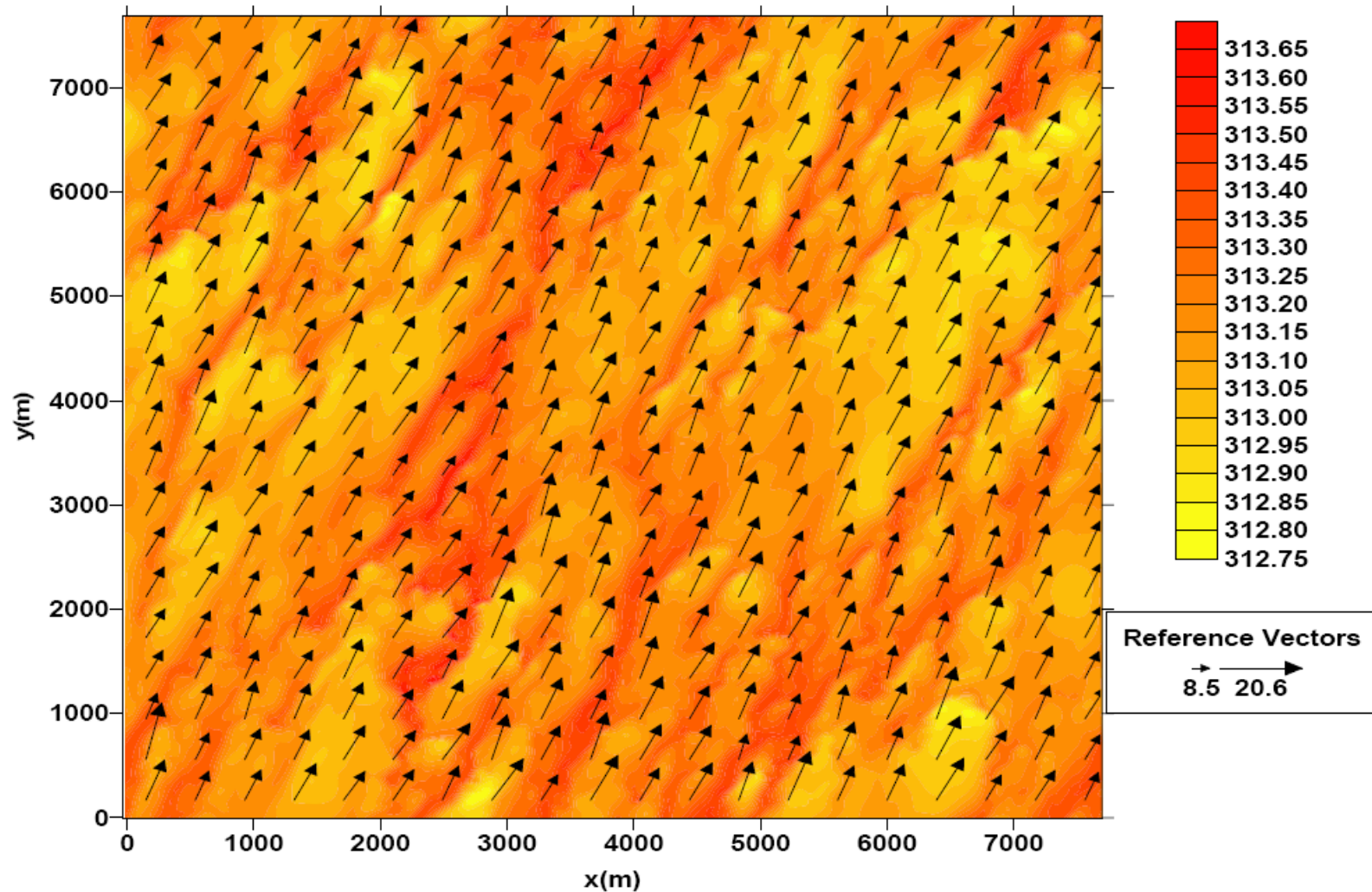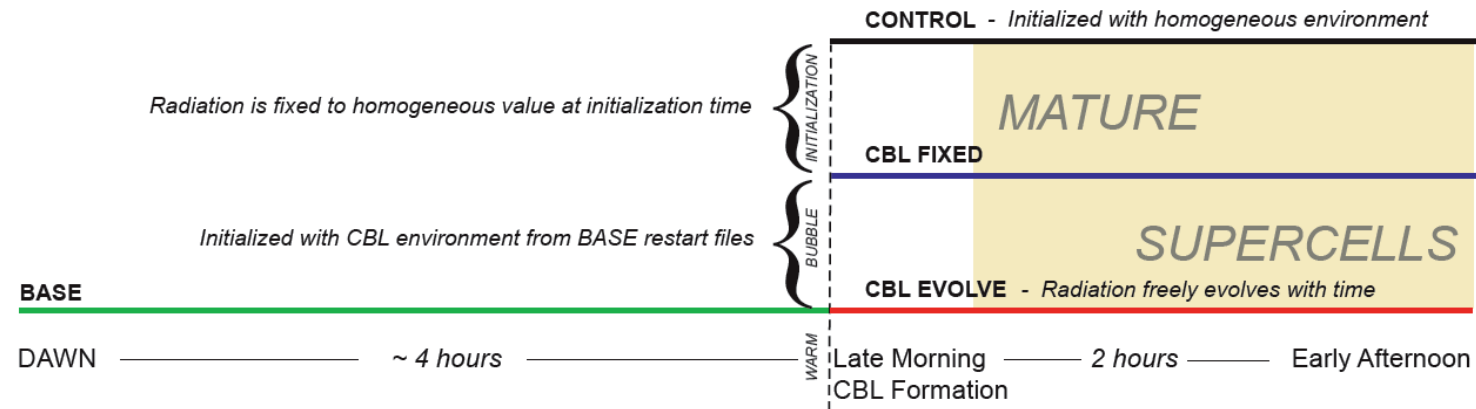
Conzemius and Fedorovich, MWR (2008)

FIG. 13. The x–y cross section at 15 m above the surface showing potential temperature (K) and horizontal wind vectors (m s^{-1}) at 1950 UTC in the simulation.

Interaction of simulated supercell with CBL rolls

Courtesy of Chris Nowotarski

All simulations are run using CM1, Release 15 (Bryan and Fritsch 2002, Bryan 2002). CM1 is a moist non-hydrostatic model that solves the compressible governing equations using a split time step, with terms associated with acoustic waves solved on a time step that is 1/6 of the large time step for non-accoustic terms (Klemp and Wilhelmson 1978). In all simulations, fifth-order advection with implicit diffusion is used. Subgrid scale turbulence is modeled using a simplified 1.5-order turbulence kinetic energy (TKE) scheme (Deardorff 1980). Cloud microphysics and precipitation are modeled using the bulk ice phase microphysical parameterization developed by Lin et al. (1983) and further modified by Tao and Simpson (1993). The Coriolis force is ignored in these simulations because its effects are negligible over the relatively short (2-hour) supercell simulation time period. The simulations include parameterizations for long and shortwave radiation (Chou and Suarez 1999), a slab soil model, surface drag, as well as surface heat and moisture fluxes.

Structure of simulated CBL rolls

Courtesy of Chris Nowotarski

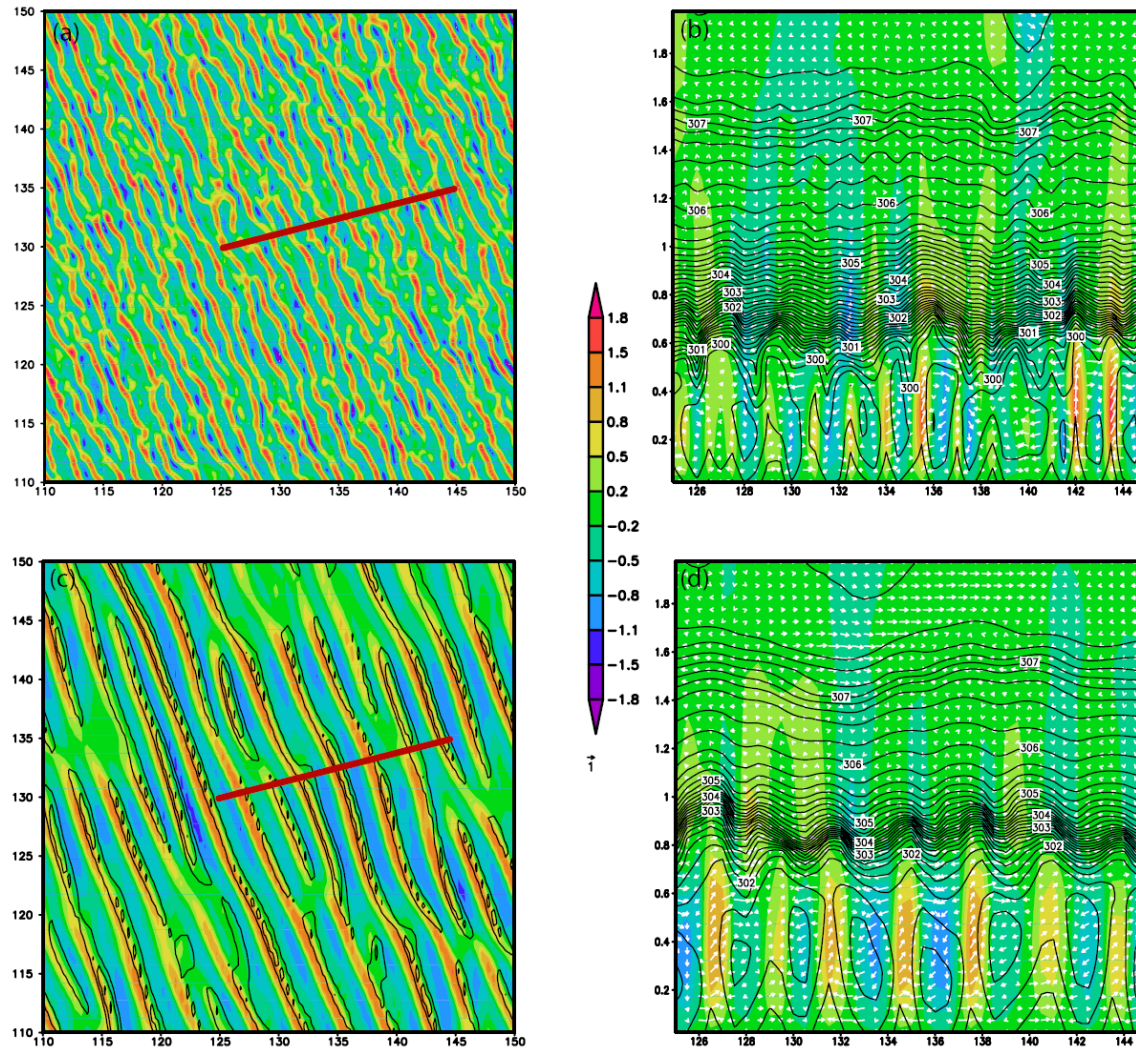Figure 4: Horizontal cross sections of vertical velocity at z = 250 m in (a) the 200-m resolution simulation, and (c) 500-m resolution simulations. The red line indicates where vertical cross sections for the (b) 200-m resolution case and the (d) 500-m resolution case are taken. Shading is vertical velocity in m s^{-1}, theta is contoured in (b) and (d) and perturbation velocity are vectors of m s^{-1} according to the legend. (c) also shows the 0.0025 s^{-1} and 0.005 s^{-1} contours of vertical vorticity at 25 m AGL.

Development of cell moving across CBL rolls

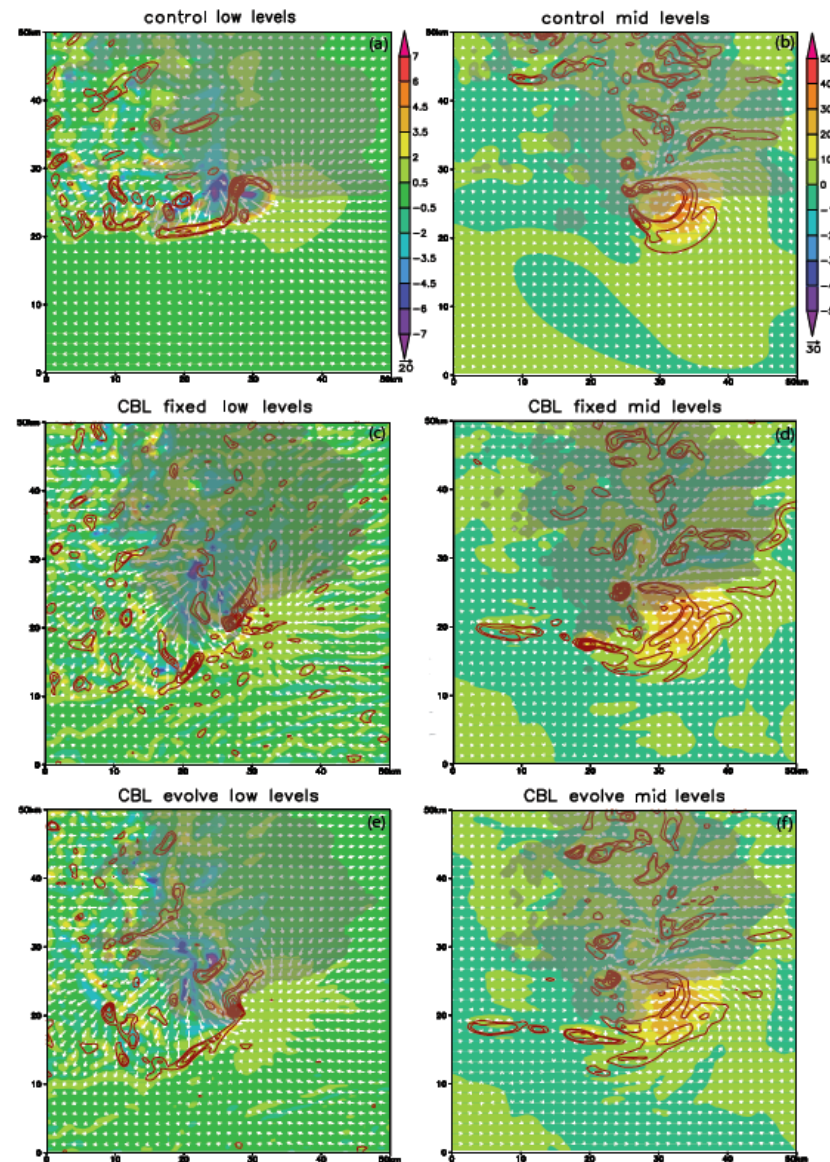**Courtesy of Chris Nowotarski**
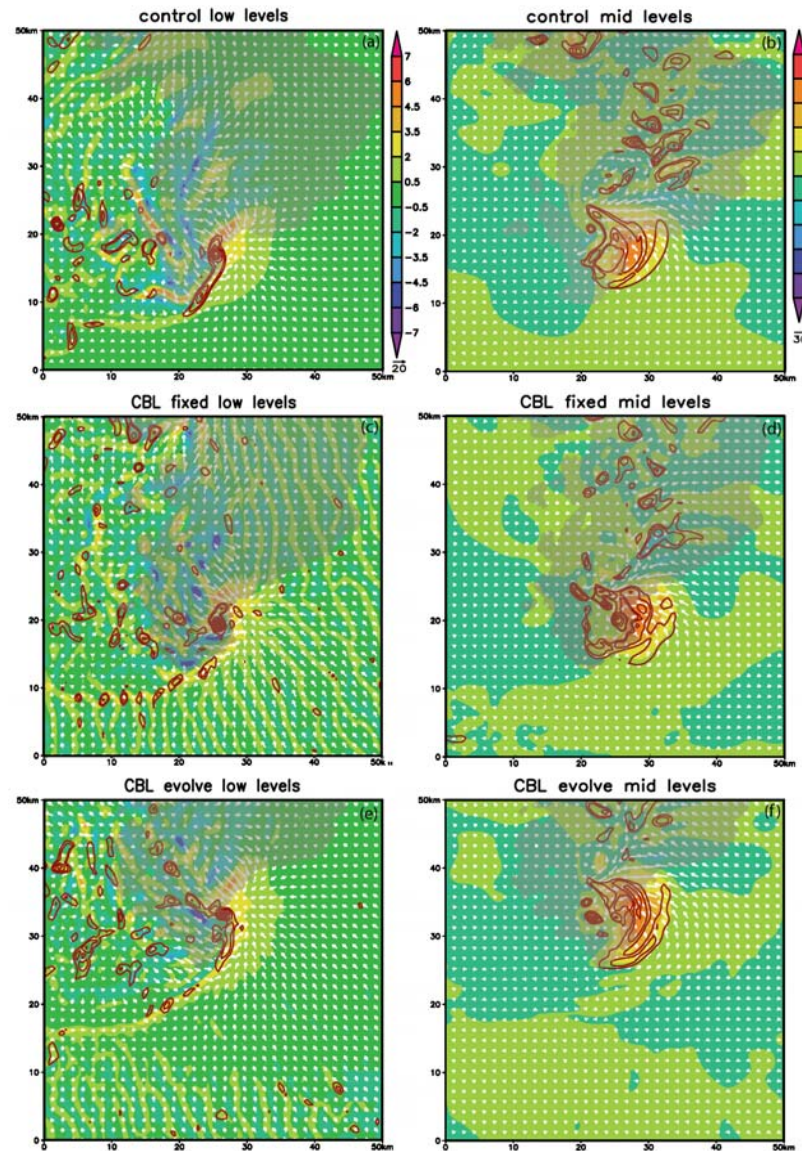
(X, Y) cross sections of vertical velocity at 275 m AGL (shaded), vertical vorticity at 25 m AGL (red), from 0.005 s⁻¹ at 0.005 s⁻¹ intervals in (a,c,e), and at 4 km AGL from 0.01 s⁻¹ at 0.01 s⁻¹ intervals in (b,d,f) Simulated reflectivity >0 dbz at 1 km AGL is in transparent gray.
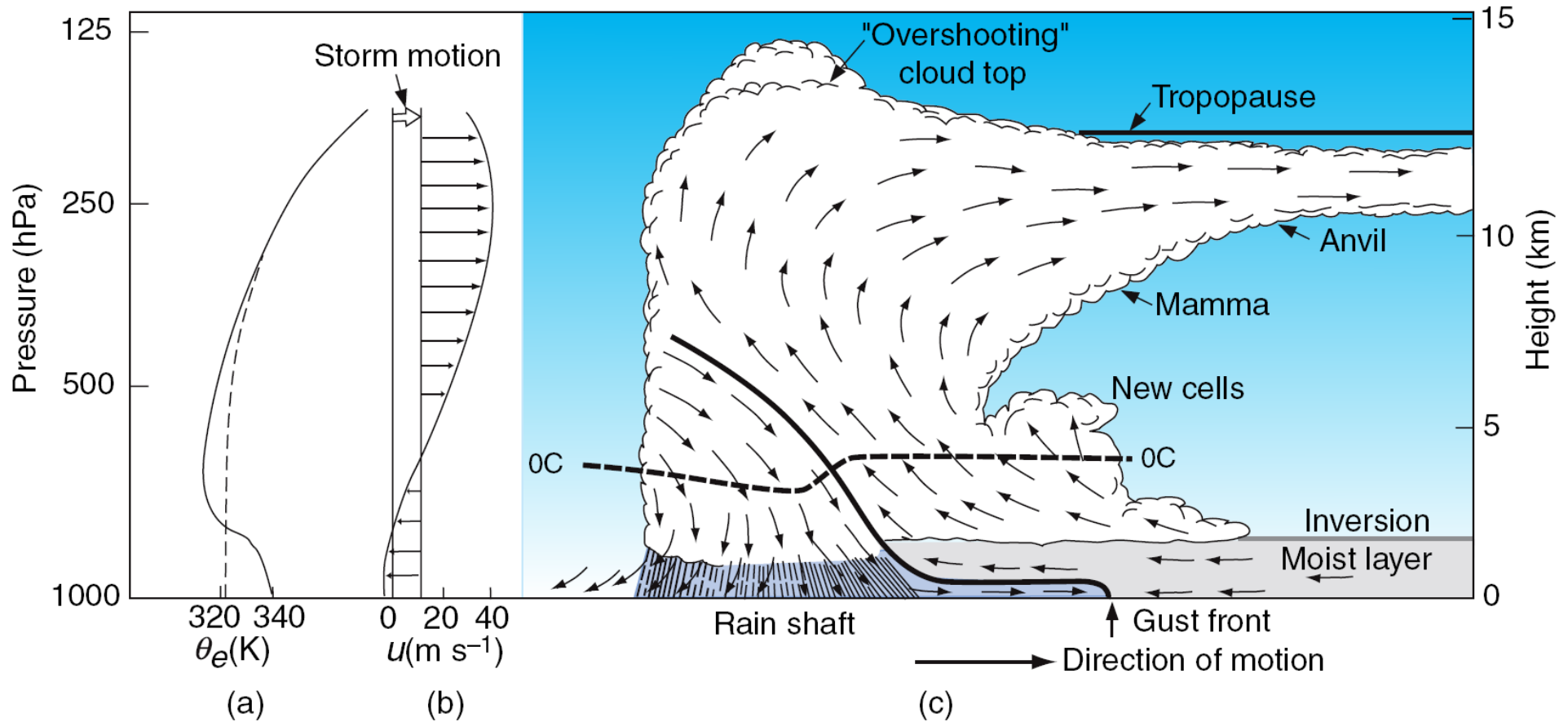
Development of cell moving along CBL rolls

Courtesy of Chris Nowotarski

(X, Y) cross sections of vertical velocity at 275 m AGL (shaded), vertical vorticity at 25 m AGL (red), from 0.005 s⁻¹ at 0.005 s⁻¹ intervals in (a,c,e), and at 4 km AGL from 0.01 s⁻¹ at 0.01 s⁻¹ intervals in (b,d,f) Simulated reflectivity >0 dbz at 1 km AGL is in transparent gray.

From

to another type of convective weather:

dust devils!

Dust devils

Courtesy of Junshi Ito

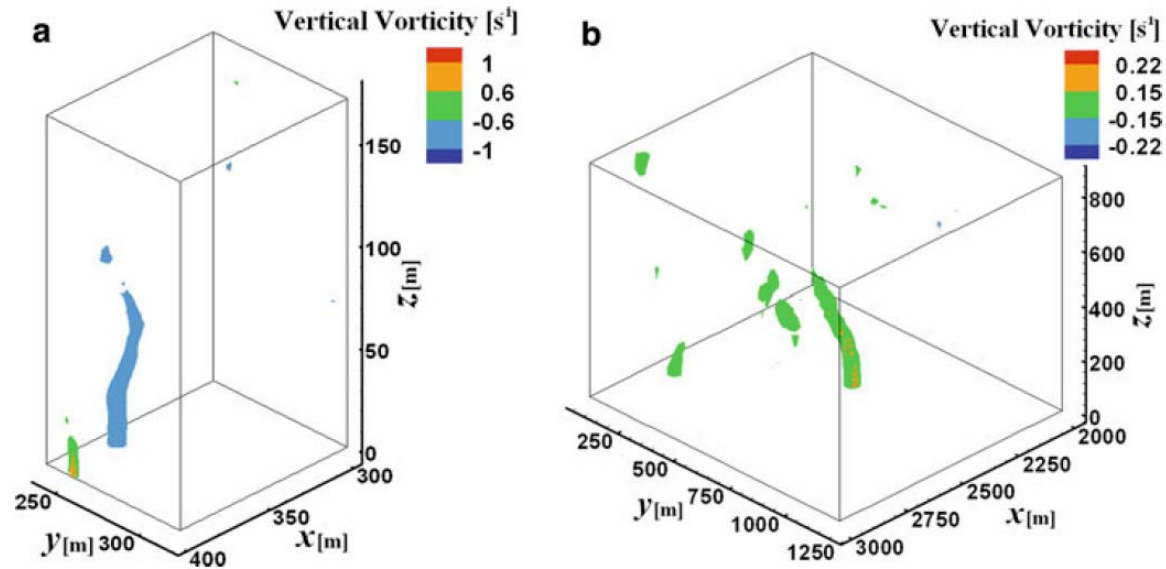# LESimulated dust devils on Earth and Mars

Gheynani and Taylor (2010)

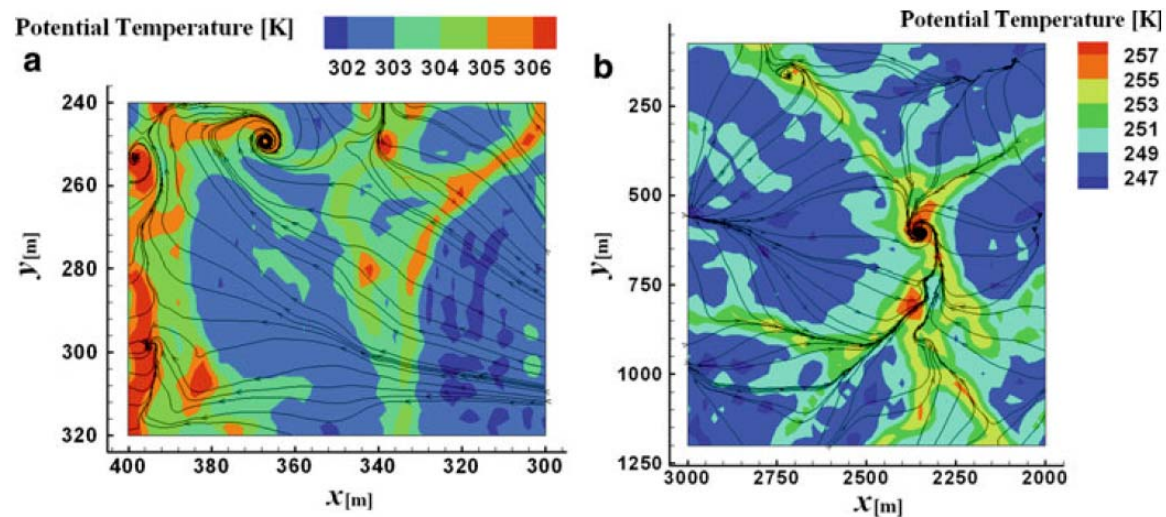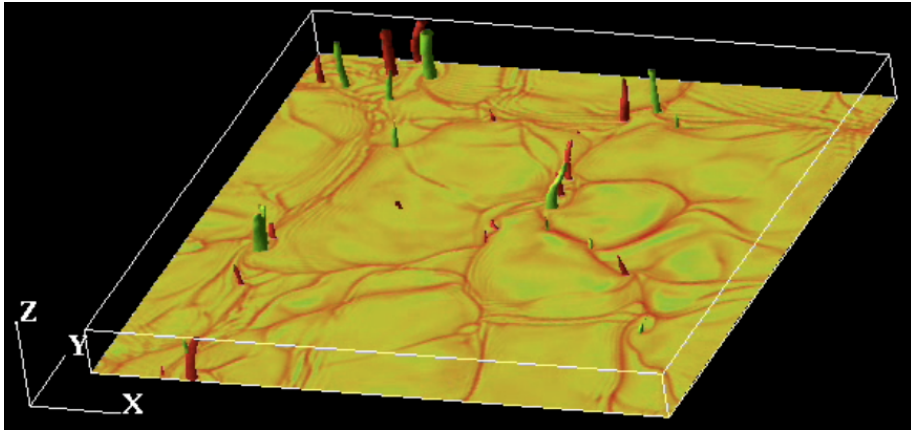Fig. 4 Vorticity volume contour plot a Earth at 1850 s, b Mars at 2298 s, simulated time

Fig. 5 Potential temperature contour plot and stream traces a Earth at 1850 s and $z = 3$ m, b Mars at 2298 s and $z = 20$ m

Effect of ambient rotation on dust devils
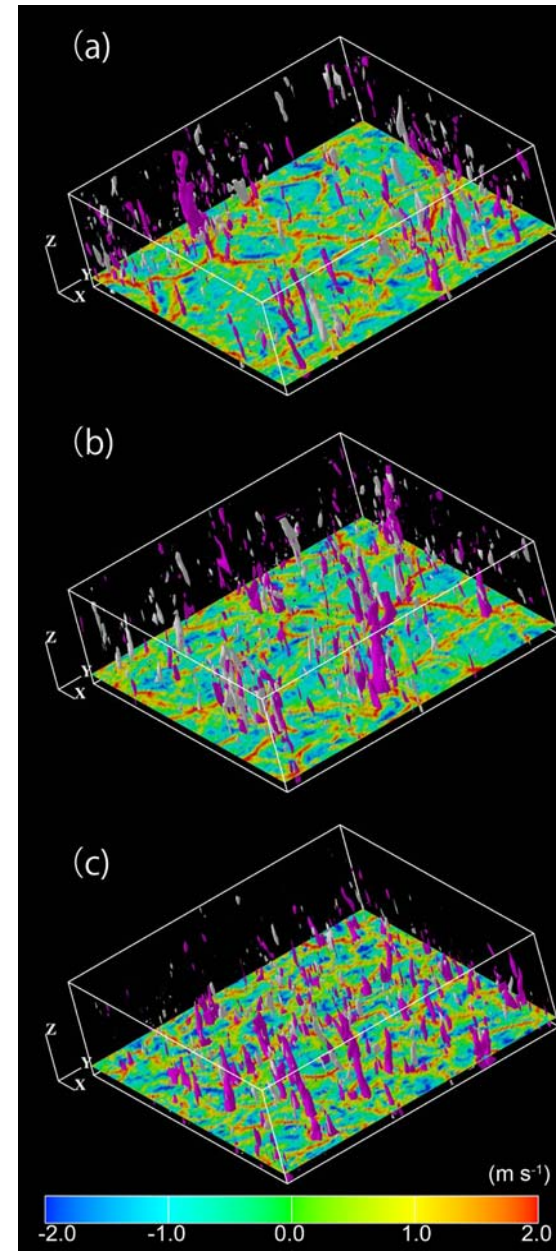
Ito et al. (2011)

Dust devils in LES domain

(a)→

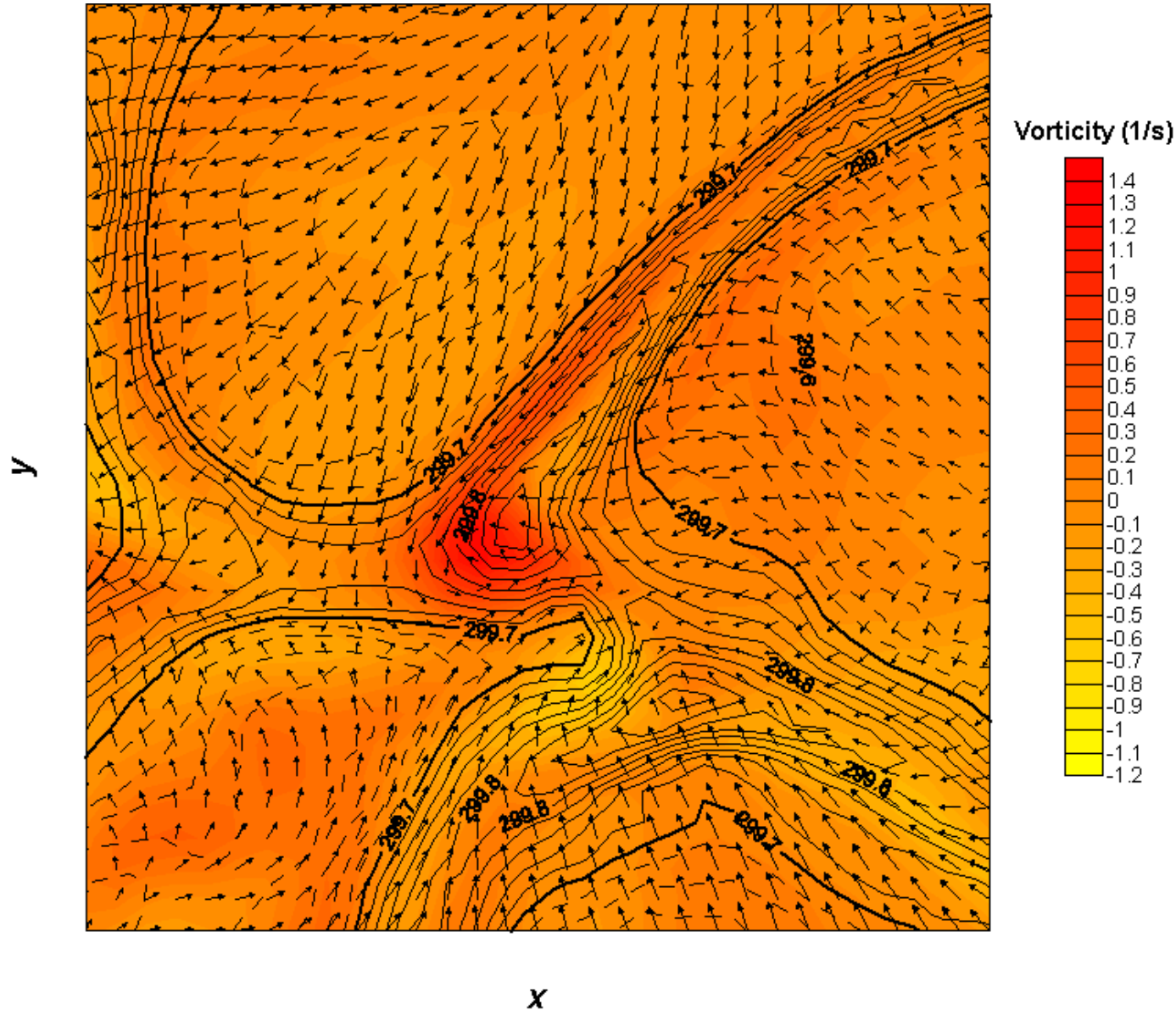ω_a **ambient =** ω_p **planetary**

(b)→

ω_a **= 10** ω_p

(c)→

ω_a **= 100** ω_p

Converting flow and vorticity in DNS of CBL

Thanks to Jeremy Gibbs (my Ph.D. student, OU)